Active Fluctuations of the Nuclear Envelope Shape the Transcriptional Dynamics in Oocytes

Maria Almonacid, Adel Al Jord, Stephany El-Hayek, Alice Othmani, Fanny Coulpier, Sophie Lemoine, Kei Miyamoto, Robert Grosse, Christophe Klein, Tristan Piolot, et al.

Article

Developmental Cell

Active Fluctuations of the Nuclear Envelope Shape the Transcriptional Dynamics in Oocytes

Graphical Abstract

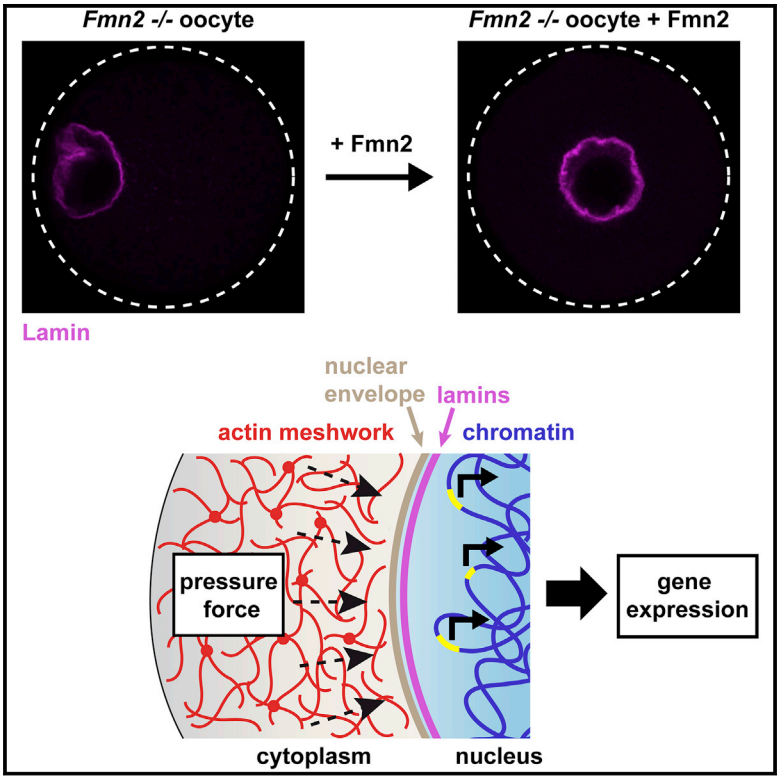

Authors

Maria Almonacid, Adel Al Jord, Stephany El-Hayek, ..., Raphaël Voituriez, Auguste Genovesio, Marie-Hélène Verlhac

Correspondence

auguste.genovesio@ens.fr (A.G.), marie-helene.verlhac@college-de-france.fr (M.-H.V.)

In Brief

Almonacid et al. show that the positioning of the nucleus in the center of the oocyte is essential for proper gene expression. Actin, which positions the nucleus centrally, also ensures proper nuclear shape, and promotes nuclear envelope and chromatin movements that fine-tune gene expression.

Highlights

- Formin 2-nucleated F-actin impacts both oocyte nuclear position and architecture
- Cytoplasmic F-actin promotes nuclear envelope fluctuations
- Nuclear envelope fluctuations impact chromatin motion inside the nucleus
- Cytoskeleton-induced nuclear envelope fluctuations modulate the oocyte transcriptome

Almonacid et al., 2019, Developmental Cell *51*, 1–13
October 21, 2019
https://doi.org/10.1016/j.devcel.2019.09.010

CellPress

Please cite this article in press as: Almonacid et al., Active Fluctuations of the Nuclear Envelope Shape the Transcriptional Dynamics in Oocytes, Developmental Cell (2019), https://doi.org/10.1016/j.devcel.2019.09.010

Developmental Cell
Article

Active Fluctuations of the Nuclear Envelope Shape the Transcriptional Dynamics in Oocytes

Maria Almonacid,[1] Adel Al Jord,[1] Stephany El-Hayek,[1] Alice Othmani,[2] Fanny Coulpier,[2] Sophie Lemoine,[2] Kei Miyamoto,[3] Robert Grosse,[4,5] Christophe Klein,[6] Tristan Piolot,[1] Philippe Mailly,[1] Raphaël Voituriez,[7] Auguste Genovesio,[2,*] and Marie-Hélène Verlhac[1,8,*]

[1]CIRB, Collège de France/CNRS-UMR7241/INSERM-U1050, PSL Research University, Equipe Labellisée FRM, Paris 75005, France
[2]Ecole Normale Supérieure, Institut de Biologie de l'ENS, IBENS/CNRS-UMR8197/INSERM-U1024, PSL Research University, Paris 75005, France
[3]Laboratory of Molecular Developmental Biology, Faculty of Biology-Oriented Science and Technology, Kindai University, Wakayama 649-6493, Japan
[4]Institute of Pharmacology, University of Freiburg, 79104 Freiburg, Germany
[5]CIBSS - Centre for Integrative Biological Signaling Studies, University of Freiburg, 79104 Freiburg, Germany
[6]Centre de Recherche des Cordeliers, CNRS, UMRS 1138/ INSERM/ UPMC, Paris 75006, France
[7]CNRS-UMR 7600 and 8237/UPMC, Paris 75005, France
[8]Lead Contact
*Correspondence: auguste.genovesio@ens.fr (A.G.), marie-helene.verlhac@college-de-france.fr (M.-H.V.)
https://doi.org/10.1016/j.devcel.2019.09.010

SUMMARY

Nucleus position in cells can act as a developmental cue. Mammalian oocytes position their nucleus centrally using an F-actin-mediated pressure gradient. The biological significance of nucleus centering in mammalian oocytes being unknown, we sought to assess the F-actin pressure gradient effect on the nucleus. We addressed this using a dedicated computational 3D imaging approach, biophysical analyses, and a nucleus repositioning assay in mouse oocytes mutant for cytoplasmic F-actin. We found that the cytoplasmic activity, in charge of nucleus centering, shaped the nucleus while promoting nuclear envelope fluctuations and chromatin motion. Off-centered nuclei in F-actin mutant oocytes were misshaped with immobile chromatin and modulated gene expression. Restoration of F-actin in mutant oocytes rescued nucleus architecture fully and gene expression partially. Thus, the F-actin-mediated pressure gradient also modulates nucleus dynamics in oocytes. Moreover, this study supports a mechano-transduction model whereby cytoplasmic microfilaments could modulate oocyte transcriptome, essential for subsequent embryo development.

INTRODUCTION

The position of the nucleus within a cell can exert a morphogenetic influence conveying spatial and temporal information (for review, see Gundersen and Worman, 2013). In many oocytes, the location of the nucleus marks the animal pole and in *Drosophila*, it defines the future dorso-ventral axis of the embryo and adult (van Eeden and St Johnston, 1999; Riechmann and Ephrussi, 2001; Roth, 2003). In mouse and humans, however, the oocyte nucleus is centrally located at the end of oocyte growth, and oocytes display no sign of polarity (FitzHarris et al., 2007; Halet and Carroll, 2007). Thus, nuclear position in mammalian oocytes does not instruct the future embryo axis. Nevertheless, an off-centered nucleus correlates with a poor outcome of oocyte development (Brunet and Maro, 2007; Levi et al., 2013), arguing that central positioning is important. This is enigmatic since fully grown oocytes subsequently undergo two asymmetric divisions, requiring an off-centering of their chromosomes (Verlhac et al., 2000). Deciphering the biological significance of nucleus centering in mammalian oocytes is, therefore, of fundamental importance.

Mouse oocytes lack canonical microtubule-organizing centers and, in contrast to neurons or *Drosophila* oocytes (Gundersen and Worman, 2013; Roth and Lynch, 2009), do not use centrosome-based nucleus positioning. Instead, they push their nucleus to the center via an actin-based mechanism (Almonacid et al., 2015). We previously described the nucleus centering mechanism in mouse oocytes (Almonacid et al., 2015) by studying oocytes from the Formin 2 (*Fmn2*) knockout strain, which lack microfilaments in their cytoplasm and present off-centered nuclei (Dumont et al., 2007a; Azoury et al., 2011). Expressing Formin 2 in $Fmn2^{-/-}$ oocytes rescues the formation of an F-actin cytoplasmic mesh that induces the motion of the nucleus toward the center (Almonacid et al., 2015). An effective pressure gradient, mediated by Formin 2-nucleated F-actin vesicles allows nucleus centering such that, at steady state, the forces are balanced, and the nucleus remains central (Almonacid et al., 2015).

To shed light on the role of nucleus centering in mammalian oocytes, we assessed the effects of the F-actin pressure gradient on the nucleus in mouse Prophase I oocytes. We discovered that nuclear architecture and dynamics were altered in oocytes lacking cytoplasmic F-actin. We developed a computational imaging approach that together with biophysical modeling show that F-actin-mediated activity, in addition to modulating nuclear shape, increased nuclear envelope fluctuations and enhanced nuclear chromatin diffusion. These nuclear

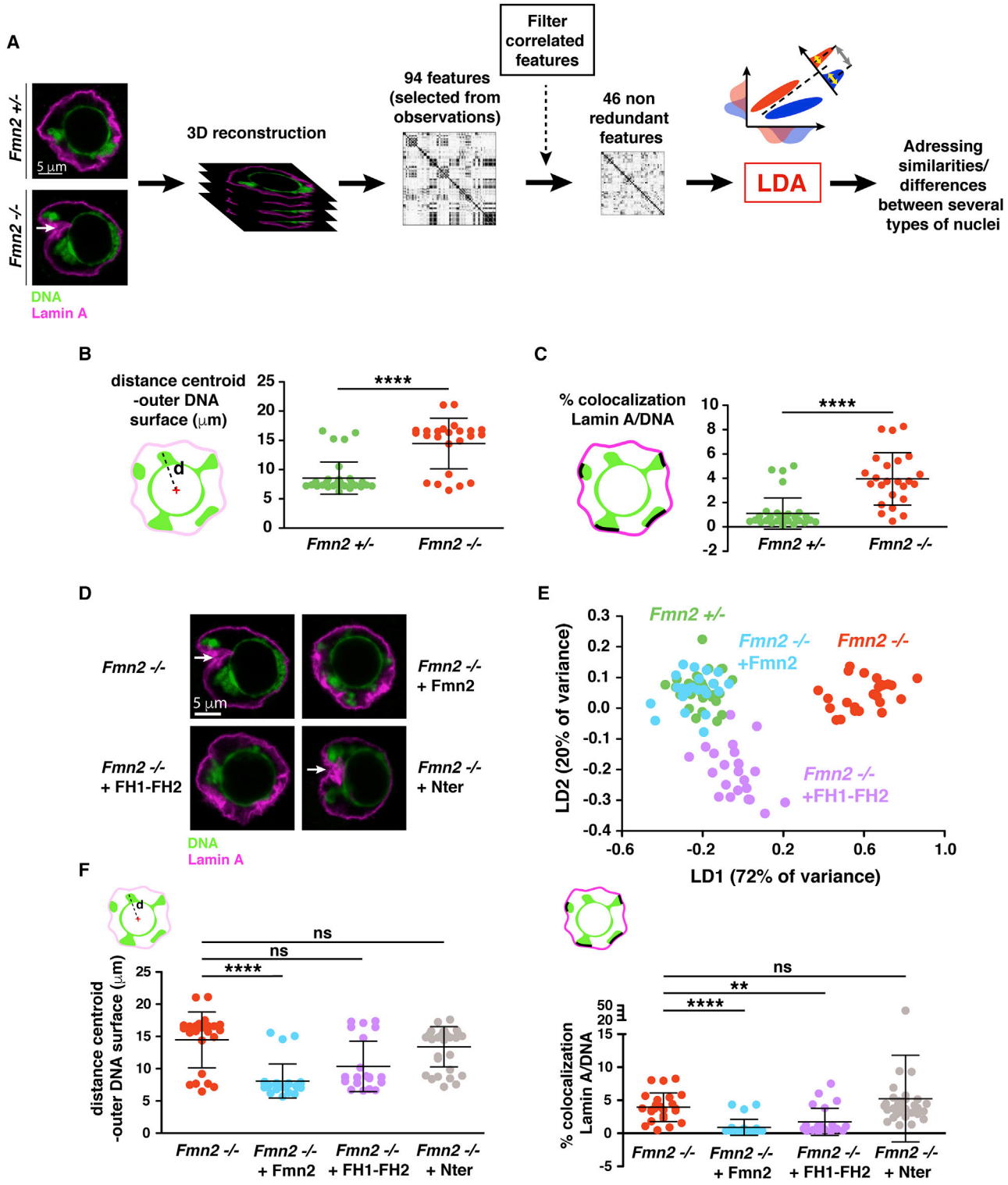

Figure 1. Nuclear Architecture Depends on Formin 2

(A) Methodology of the computational imaging approach. Oocytes were stained for Lamin A (magenta) and DNA (green), as shown on the single plane images of a *Fmn2*$^{+/-}$ and a *Fmn2*$^{-/-}$ nucleus (respectively top and bottom left panels). The white arrow points to the invagination observed in *Fmn2*$^{-/-}$ nuclei. Scale bar is 5 µm. The nuclei were reconstructed in 3D and analyzed using the computational imaging approach schematized (see STAR★Methods).

(B) Nuclear architecture is perturbed in *Fmn2*$^{-/-}$ compared to *Fmn2*$^{+/-}$ oocytes. Measure of the feature « DNA dispersion » extracted from the computational imaging approach. Left, scheme of the methodology of the DNA dispersion measure, corresponding to the distance from the centroid to the outer surface of the

(legend continued on next page)

differences were associated with deregulated gene expression impacting all chromosomes and arguing for a global transcriptional effect. Nuclear alterations were reversible, whereas gene expression profiles were rescuable to some extent. Thus, cytoplasmic microfilaments potentially modulate nucleus dynamics in the oocyte and could preserve maternal RNA stockpiles to sustain early embryonic development.

RESULTS

Nucleus Architecture Differs in Formin 2-Mutant Oocytes Devoid of Cytoplasmic F-Actin

We showed that cytoplasmic microfilament forces center the mouse oocyte nucleus and suggested that these forces may affect nuclear shape (Almonacid et al., 2015). To confirm this observation, we assessed nuclear architecture in control *Fmn2*$^{+/-}$ versus *Fmn2*$^{-/-}$ Prophase I-arrested oocytes. We stained chromatin and Lamin A in the two oocyte types (Figure 1A, left images). The nucleus of *Fmn2*$^{-/-}$ oocytes presented an important smooth surface and a major invagination that was never observed in controls (Figure 1A, bottom left image, white arrow). Despite the presence of this invagination in *Fmn2*$^{-/-}$ nuclei, the Lamin A staining was uniform along the nuclear envelope, and the intensity of this staining was comparable to controls, suggesting, yet not proving (Deviri et al., 2019), that nuclear integrity was unaffected (Figure 1A, left images). To further address the integrity of the nuclear envelope in *Fmn2*$^{-/-}$ oocytes, we used a nucleo-plasmic probe (YFP-Rango, Figure S1A) that leaks out of the nucleus when nuclear envelope permeability increases (Azoury et al., 2011). The nucleo-cytoplasmic ratio of fluorescence of the probe did not differ between control and *Fmn2*$^{-/-}$ oocytes, arguing in favor of an intact nuclear envelope in both cases (Figure S1B). To quantify potential differences in nuclear architecture between *Fmn2*$^{+/-}$ and *Fmn2*$^{-/-}$oocytes, we developed a computational imaging approach to automatically threshold the stacks of images and extracted 46 non-redundant features characterizing the nucleus (shape, volume, DNA dispersion: Figure 1A and STAR Methods for feature list). Among these features, which varied significantly between control and *Fmn2*$^{-/-}$oocytes, was an increased DNA dispersion along with a higher distance of the DNA centroid to the outer DNA surface (Figure 1B), in spite of a comparable nuclear size (mean and SD of nuclear volume of 3,485 ± 708.3 μm^3 for *Fmn2*$^{+/-}$ and 3,867 ± 1,857 μm^3 for *Fmn2*$^{-/-}$, not significant; Mann-Whitney U p = 0.48). Another feature of interest was the significant increase in contact between DNA and Lamin A in *Fmn2*$^{-/-}$ oocytes compared to controls, possibly due to the observed nucleus indentation (Figure 1C). Altogether, these data suggest that a lack of Formin 2 in oocytes leads to nuclear architectural defects without nuclear integrity perturbations.

Formin 2 Rescues Nuclear Architecture in *Fmn2*$^{-/-}$ Oocytes

To further assess the link between Formin 2 and nuclear architecture defects, we injected *Fmn2*$^{-/-}$oocytes with RNAs encoding full-length Formin 2, the actin-nucleating domain of Formin 2 (FH1-FH2 domain; Kovar, 2006), or the N-terminal part of Formin 2, which does not nucleate actin (Figure S2A). Only the full-length (Almonacid et al., 2015) and the FH1-FH2 domain of Formin 2, which have the ability to nucleate actin, could rescue the nucleus central position (Figure S2B). We analyzed the evolution of nuclear architecture in injected oocytes using our dedicated computational 3D imaging approach. Both full-length and FH1-FH2 restored the spherical shape of nuclei (Figures 1D and S2B) and the percentage of contacts with Lamin A (Figure 1F; right panel) to levels comparable to controls. Full-length Formin 2 rescued the spreading of DNA inside the nucleus (Figure 1F, left panel) while the FH1-FH2 was less efficient for this feature (Figure 1F, left panel), highlighting that the FH1-FH2 domain does not fully recapitulate all Formin 2 endogenous interactions. The perfect rescue of nuclear architecture by full-length Formin 2 was also attested by the linear discriminant analysis (LDA) (Figure 1E). LDA is a modified form of the principal component analysis, allowing to compare samples based on the statistical

DNA mass. Error bars represent SD. Mean and SD are 8.55 ± 2.74 μm for *Fmn2*$^{+/-}$ and 14.47 ± 4.33 μm for *Fmn2* $^{-/-}$. Mann-Whitney U p value = 8.06E-06. n=35 oocytes for *Fmn2*$^{+/-}$and n=24 oocytes for *Fmn2*$^{-/-}$, 2 independent experiments.

(C) Nuclear architecture is perturbed in *Fmn2*$^{-/-}$ compared to *Fmn2*$^{+/-}$ oocytes. Measure of the feature « overlap between Lamin A and DNA » extracted from the computational imaging approach. Left: scheme of the methodology of the measure of overlap between Lamin A and DNA, which is the percentage of colocalization of Lamin A and DNA related to the total DNA. Error bars represent SD. Mean and SD are 1.1 ± 1.28 for *Fmn2*$^{+/-}$ and 3.95 ± 2.16 for *Fmn2*$^{-/-}$. Mann-Whitney U p value = 2.55E-07. n=35 oocytes for *Fmn2*, n=24 oocytes for *Fmn2*$^{-/-}$, 2 independent experiments.

(D) Nuclear architecture in *Fmn2*$^{-/-}$ and in the 3 different rescue conditions. Single plane images of nuclei stained for Lamin A (magenta) and DNA (green) in *Fmn2*$^{-/-}$ (top left), *Fmn2*$^{-/-}$ expressing either the full-length Formin 2 (Fmn2, top right), the FH1-FH2 domain (FH1-FH2, bottom left) or the N-terminal domain (Nter, bottom right). White arrows point to the invaginations observed in nuclei from *Fmn2*$^{-/-}$ and *Fmn2* $^{-/-}$ expressing the N-terminal domain. Scale bar is 5 μm.

(E) Nuclear architecture is regulated by nucleus centering. Linear discriminant analysis (LDA) of the 4 different types of nuclei: *Fmn2*$^{+/-}$, *Fmn2*$^{-/-}$, *Fmn2*$^{-/-}$ + full-length Formin 2 and *Fmn2*$^{-/-}$ + FH1-FH2 domain (see Figure 1A and STAR★Methods). n=35 for *Fmn2*$^{+/-}$, 2 independent experiments, n=24 for *Fmn2*$^{-/-}$, 2 independent experiments, n=26 for Fmn2$^{-/-}$ + Fmn2, one experiment, n=23 for *Fmn2*$^{-/-}$ + FH1-FH2, one experiment.

(F) Full-length Formin 2 and the FH1-FH2 domain of Formin 2 rescue the co-localization of DNA with Lamin A. Measure of the extent of rescue of nuclear architecture of *Fmn2*$^{-/-}$ oocytes by full-length Formin 2, by the FH1-FH2 domain and by the N-terminal domain for the 2 features « DNA dispersion » and « overlap between Lamin A and DNA » from the computational imaging approach described in Figure 1A. Left: DNA dispersion, measured by the distance from the centroid to the outer surface of the DNA mass. Error bars represent SD. Mean and SD are 14.47 ± 4.33 μm for *Fmn2*$^{-/-}$, 8.09 ± 2.64 μm for *Fmn2*$^{-/-}$ + Fmn2, 10.36 ± 3.90 μm for *Fmn2*$^{-/-}$ + FH1-FH2 and 13.38 ± 3.13 μm for *Fmn2*$^{-/-}$ + Nter. Mann-Whitney U p values are 7.2E-06 for *Fmn2*$^{-/-}$ - *Fmn2*$^{-/-}$ + Fmn2, 3.33E-02 for *Fmn2*$^{-/-}$ - *Fmn2*$^{-/-}$+ FH1-FH2 and 4.62E-02 for *Fmn2*$^{-/-}$ - *Fmn2*$^{-/-}$ + Nter. n=24 for *Fmn2*$^{-/-}$, 2 independent experiments, n=26 for *Fmn2*$^{-/-}$ + Fmn2, one experiment, n=23 for *Fmn2*$^{-/-}$ + FH1-FH2, one experiment and n=32 for *Fmn2*$^{-/-}$ + Nter, 2 independent experiments. Right: overlap between Lamin A and DNA, measured by the percentage of co-localization of Lamin A and DAPI related to the total DNA. Error bars represent SD. Mean and SD are 3.95 ± 2.16 for *Fmn2*$^{-/-}$, 0.91 ± 1.19 for *Fmn2*$^{-/-}$ + Fmn2, 1.74 ± 2.05 for *Fmn2*$^{-/-}$ + FH1-FH2 and 5.24 ± 6.56 for *Fmn2*$^{-/-}$ + Nter. Mann-Whitney U p values are 8.58E-07 for *Fmn2*$^{-/-}$ - *Fmn2*$^{-/-}$ + Fmn2, 8.16E-04 for *Fmn2*$^{-/-}$ - *Fmn2*$^{-/-}$ + FH1-FH2 and 8.01E-01 for *Fmn2*$^{-/-}$ - *Fmn2*$^{-/-}$ + Nter. n=24 for *Fmn2*$^{-/-}$, 2 independent experiments, n=26 for *Fmn2*$^{-/-}$ + Fmn2, one experiment, n=23 for *Fmn2*$^{-/-}$ + FH1-FH2, one experiment and n=32 for *Fmn2*$^{-/-}$ + Nter, 2 independent experiments.

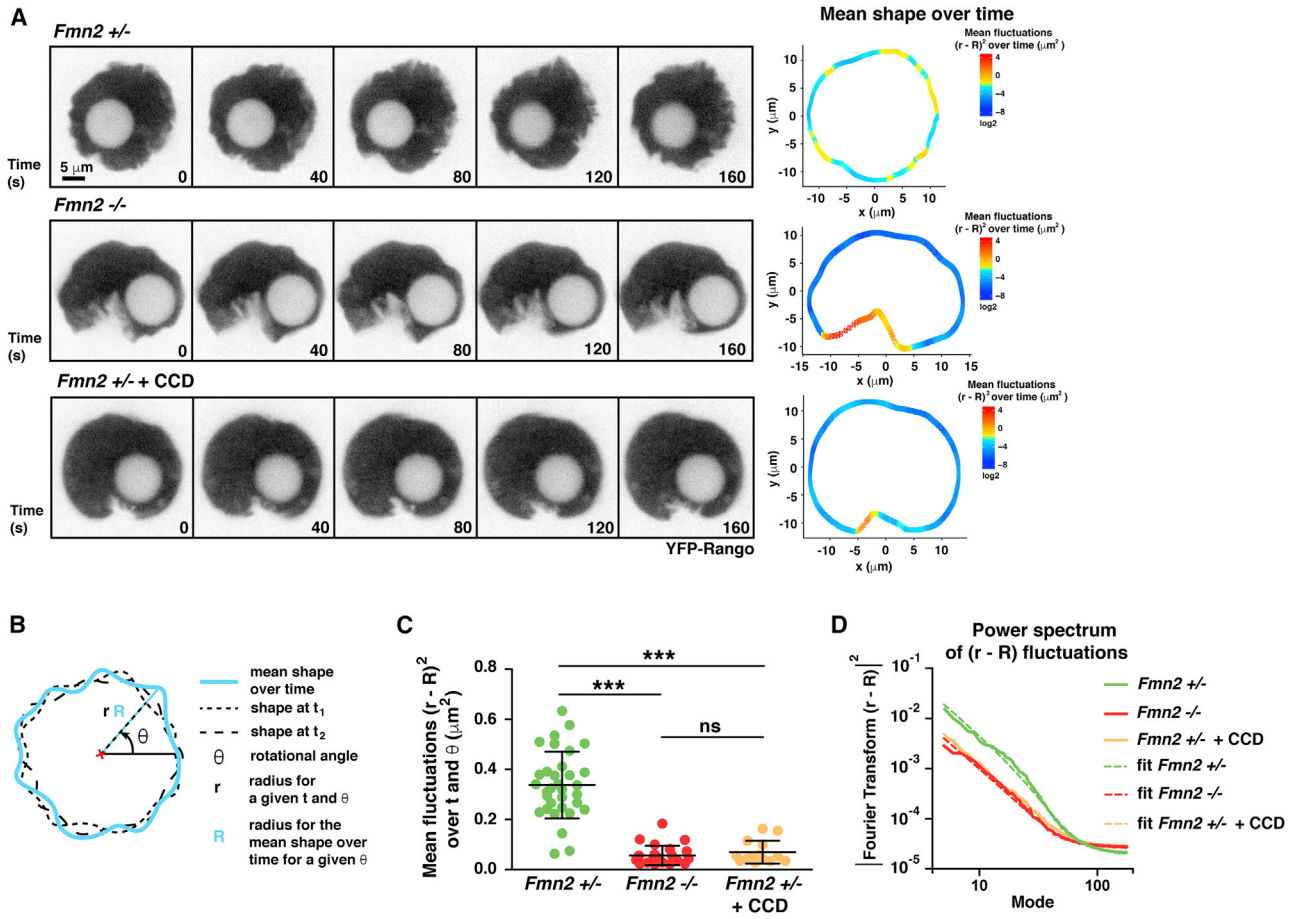

Figure 2. Formin 2-Nucleated Actin Filaments Induce Nuclear Envelope Fluctuations

(A) Actin induced cytoplasmic activity impacts on nuclear envelope fluctuations and nuclear shape. Left: images from a movie of a $Fmn2^{+/-}$ (top), $Fmn2^{-/-}$ (middle) or a $Fmn2^{+/-}$ treated with CCD (bottom) oocytes injected with cRNAs coding for the nuclear probe YFP-Rango. Scale bar is 5 μm. Right: Heatmaps of the mean nuclear outline over 5 min measured from the different oocytes of the left gallery. The color codes of heat maps represent nuclear outline fluctuations in μm^2, for each position along the circumference relative to the mean shape over time. Red is for highest and blue for lowest fluctuation values.

(B) Scheme of the method used to quantify nuclear envelope fluctuations over time and in a given direction. Directions were defined by a revolving angle θ of a 1° increment from 0 to 360°. Mean and variance of the radius distribution in a given direction were computed for each direction and reported as a schematic plot (heatmaps on Figure 2A right) where the radius of the membrane represents the mean and the color on the membrane represents the corresponding variance.

(C) Nuclear envelope fluctuations are perturbed in both $Fmn2^{-/-}$ and $Fmn2^{+/-}$ + CCD oocytes. Nuclear fluctuations over 5 min, represented by the variance of the radius over t and θ, from $Fmn2^{+/-}$ (green), $Fmn2^{-/-}$ (red) and $Fmn2^{+/-}$ + CCD (orange) nuclei. For $Fmn2^{-/-}$ and $Fmn2^{+/-}$ + CCD, the region of the large invagination was excluded from the measurements. Error bars represent SD. Mean and SD 0.34 ± 0.13 μm^2 for $Fmn2^{+/-}$, 0.057 +/−0.038 μm^2 for $Fmn2^{-/-}$ and 0.07 ± 0.04 μm^2 for $Fmn2^{+/-}$ + CCD. Mann-Whitney U p values are < 0.0001 for $Fmn2^{+/-}$ - $Fmn2^{-/-}$, < 0.0001 for $Fmn2^{+/-}$ - $Fmn2^{+/-}$+ CCD and 0.2987 for $Fmn2^{-/-}$ - $Fmn2^{+/-}$ + CCD. n=33 oocytes for $Fmn2^{+/-}$, 3 experiments, n=25 oocytes for $Fmn2^{-/-}$, 3 experiments and n=14 for $Fmn2^{+/-}$+ CCD, one experiment.

(D) Power spectrum of nuclear fluctuations over 5 min: the squared moduli of the Fourier transforms of fluctuations (R-R) are plotted as a function of the mode for $Fmn2^{+/-}$ (green), $Fmn2^{-/-}$ (red) and $Fmn2^{+/-}$ + CCD (orange) nuclei. For $Fmn2^{-/-}$ and $Fmn2^{+/-}$+ CCD, the region of the large invagination was excluded from the measurements. Data are fitted to the function $1 / (\bar{\sigma}n^2 + \bar{\kappa}n^4)$ + Yinf according to the Helfrich model.

differences between features obtained from our computational biology approach (more explanations in STAR Methods). The computational approach allowed an efficient detection and quantification of nuclear architecture differences between oocytes. Thanks to this approach, we can conclude that Formin 2 modulates the architecture of the oocyte nucleus.

Actin Promotes Nuclear Envelope Fluctuations and Shapes the Nucleus

To probe the role of Formin 2 on the dynamics of nuclear shape in living oocytes, we followed the nuclear envelope contour at high temporal resolution (500 ms) in 2D using our YFP-Rango nuclear probe (Azoury et al., 2011) (as for Figure S1). As previously observed (Luksza et al., 2013), the nuclear envelope of mouse oocytes in Prophase I was highly deformable (Figure 2A upper left panel and Video S1). The nucleus in control $Fmn2^{+/-}$ oocytes was relatively round with evenly distributed deformations (Figure 2A upper left panel). Consistent with observations on fixed cells (Figure 1A), $Fmn2^{-/-}$ oocyte nuclei were no longer round, deformed, and presented 65.76% of a smooth surface (Figure 2A middle left panel and Video S1). We then compared the evolution of the nuclear shape as a function of time in control and

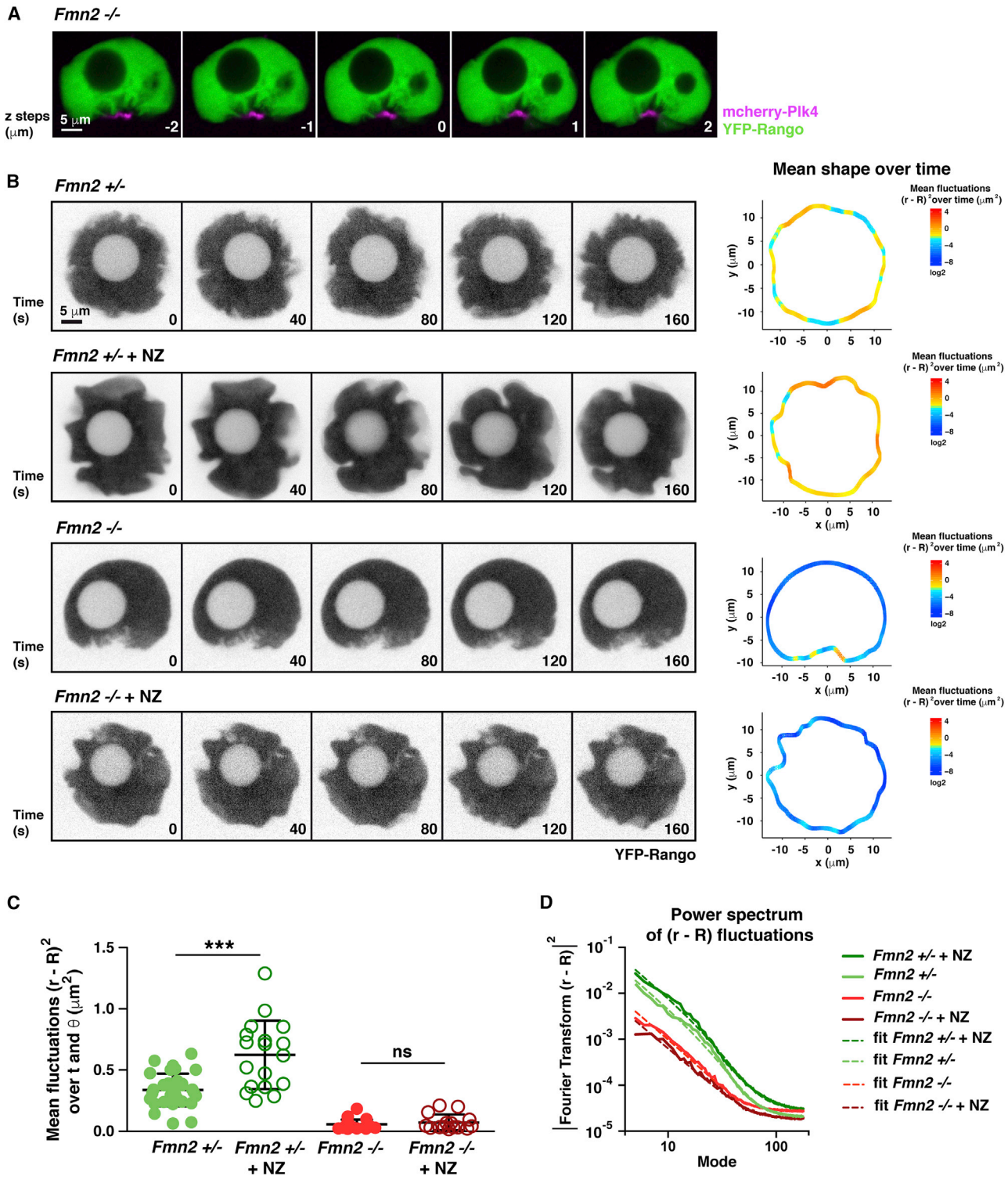

Figure 3. Microtubules Impact Nuclear Shape and Nuclear Envelope Fluctuations

(A) The invagination in *Fmn2*$^{-/-}$ nuclei contains a major aMTOC. Z-stacks spaced of 1 μm of a *Fmn2*$^{-/-}$ nucleus. The aMTOC is labeled with mCherry-Plk4 (magenta) and the nucleus is labeled with the nucleo-plasmic probe YFP-Rango (green). Scale bar is 5 μm.

(B) Treatment with NZ for 2 h increases nuclear envelope fluctuations in control oocytes and affects nuclear shape in *Fmn2*$^{-/-}$ oocytes. Left: images from movies of *Fmn2*$^{+/-}$ (top), *Fmn2*$^{+/-}$ treated with NZ (second lane), *Fmn2*$^{-/-}$(third lane) and *Fmn2*$^{-/-}$ treated with NZ (bottom) oocytes injected with cRNAs coding for the nuclear probe YFP-Rango. Scale bar is 5 μm. Heatmaps of the mean nuclear outline over 5 min measured from the different oocytes of the left gallery. The color

(legend continued on next page)

Fmn2$^{-/-}$ oocytes (Figure 2B, see STAR Methods). Controls had more regular round-shaped nuclei and a nuclear envelope subjected to more important fluctuations all along the entire surface (compare heatmaps of Figure 2A from upper versus middle right panels). The control nuclear envelope was subjected to about 6 times more important fluctuations than that of *Fmn2*$^{-/-}$ (Figure 2C). The fluctuations can be attributed to cytoplasmic actin filaments nucleated by Formin 2 since treating controls with Cytochalasin D (CCD, an actin depolymerizing drug) mimicked the shape (Figure 2A lower left panel with 66.12% of smooth surface) as well as the distribution and extent of fluctuations present in *Fmn2*$^{-/-}$ nuclei (Figure 2A lower right panel and 2C; Video S2). Hence, Formin 2-nucleated actin filaments promote nuclear envelope fluctuations and a round-shaped nucleus.

Microtubules Dampen Actin-Based Fluctuations

We suspected the implication of microtubules in the appearance of the nuclear invagination in *Fmn2*$^{-/-}$ and CCD-treated controls. Indeed, the major acentriolar MicroTubule Organizing Center (aMTOC), normally apposed to the nucleus at that developmental stage (Luksza et al., 2013), was in close proximity with the invagination (Figure 3A; Video S3). To assess further the contribution of the other major cytoskeletal component, microtubules, to nuclear shape, we treated control oocytes with a microtubule depolymerizer, Nocodazole (NZ). Despite having a comparable shape, treated cells showed an increase in nuclear envelope fluctuations (compare heatmaps of Figure 3B right panels and Video S4). The variance of these fluctuations was twice as high as that in NZ-treated than steady-state controls (Figure 3C). Interestingly, treating Formin 2 mutant oocytes with NZ removed the invagination (Figure 3B, lowest panel; Video S5). Hence, the invagination in oocytes depleted of F-actin is probably formed by tethering of microtubules emanating from the major aMTOC to the nuclear envelope. To conclude, microtubules impact nuclear shape only in the absence of F-actin. In a control situation, however, microtubules dampen actin-mediated fluctuations of the nuclear envelope.

Physical Model Describing Cytoskeleton-Based Nuclear Envelope Fluctuations

To further analyze fluctuations of the nuclear envelope and extract its physical properties, we proceeded with a modeling approach. The oocyte cytoplasm can be modeled as an active fluid (Almonacid et al., 2015). Here, the term "active" refers to non-equilibrium processes (i.e., ATP dependent) involving F-actin and microtubules, such as polymerization and depolymerization of actin and/or microtubule filaments interactions. This active fluid can be characterized in a first approximation by an effective temperature T_{cyto} = T + Ta, where T is the usual temperature, and T_a is the active temperature that accounts for the fluctuations of the F-actin network. The rheology of the nuclear envelope being largely unknown, we adopted the classical Helfrich model of membranes (Nelson et al., 1989) parameterized by a tension $\bar{\sigma}$ and a bending modulus $\bar{\kappa}$ (see model in STAR Methods). In order to confront the model to our data, we considered the radial deformations of the envelope in a 2D cross section, and parameterized the envelope by its local radial deformation h(θ,t)=r(θ,t)-R(θ), where R(θ) is the average over time of the radial coordinate r(θ,t) of the envelope at the polar angle θ (see model in STAR Methods). The fluctuations of the envelope were then analyzed by introducing the Fourier decomposition $\widehat{h_n} = \int_0^{2\pi} e^{-in\theta} h(\theta) d\theta$, which quantifies the contribution of each mode *n*. Making use of the fluctuation dissipation theorem (Kubo, 1966), the power spectrum of fluctuations is then deduced as follows (see model in STAR Methods):

$$|\widehat{h_n}|^2 = \frac{2\pi k_B T_{cyto}}{\bar{\sigma} n^2 + \bar{\kappa} n^4} \qquad \text{(Equation 1)}$$

where k_B is the Boltzmann constant, $\bar{\sigma} \propto \sigma$ is the effective tension and $\bar{\kappa} \propto \kappa / R^2$ the effective bending modulus after 2D projection, with *R,* the mean nucleus radius.

Thus, the model predicts that nuclear envelope fluctuations (quantified by the power spectrum) are controlled by the activity of the cytoplasm, which is here quantified by the active temperature T_a. Fitting the power spectrum measured experimentally by equation (1) (Figures 2D and 3D) confirmed that the nuclear envelope could be described by the Helfrich model and gave access to the characteristic length $l_c = R\sqrt{\bar{\kappa}/\bar{\sigma}}$, which is a marker of the physical properties of the nuclear envelope (note that the determination of tension and bending modulus independently is not accessible by this approach). Importantly, our analysis revealed that l_c in *Fmn2*$^{+/-}$, *Fmn2*$^{-/-}$, CCD-, and NZ-treated oocytes are relatively close in the range of 0.18–0.4 μm (Table 1). This suggested that the physical properties of the nuclear envelope are similar in all cases and led to the assumption that $\bar{\sigma}, \bar{\kappa}$ are constant. Based on this, the analysis of the power spectra showed that *Fmn2*$^{-/-}$, CCD- or NZ-treated control oocytes display significantly lower effective temperatures T_{cyto} (5-fold difference between *Fmn2*$^{+/-}$ and *Fmn2*$^{-/-}$ or CCD-treated *Fmn2*$^{+/-}$, more than 7-fold difference between *Fmn2*$^{+/-}$ and NZ-treated *Fmn2*$^{-/-}$ oocytes; Table 1). Overall, this suggests that nuclear envelope fluctuations are not due to inherent changes of its mechanical properties in the different types of oocytes but are generated by the cytoskeleton-based cytoplasmic activity.

codes of heat maps represent the nuclear outline fluctuations in μm^2, for each position along the circumference relative to the mean shape over time. Red is for highest and blue for lowest fluctuation values.

(C) Nuclear envelope fluctuations are twice higher after NZ treatment in controls. Nuclear envelope fluctuations over 5 min represented by the variance of the radius over t and θ from *Fmn2*$^{+/-}$ (light green), *Fmn2*$^{+/-}$+ NZ (dark green), *Fmn2*$^{-/-}$ (red), *Fmn2*$^{-/-}$ + NZ (dark red) nuclei. For *Fmn2*$^{-/-}$, the region of the large invagination was excluded from the measurements. Error bars represent SD. Mean and SD are 0.34 ± 0.13 μm^2 for *Fmn2*$^{+/-}$, 0.62 ± 0.28 μm^2 for *Fmn2*$^{+/-}$ + NZ, 0.057 ± 0.038 μm^2 for *Fmn2*$^{-/-}$ and 0.073 ± 0.064 μm^2 for *Fmn2*$^{-/-}$ + NZ. Mann-Whitney U p values are 0.0002 for *Fmn2*$^{+/-}$ -*Fmn2*$^{+/-}$ + NZ and 0.89 for *Fmn2*$^{-/-}$ -*Fmn2*$^{-/-}$ + NZ. n=33 oocytes for *Fmn2*$^{+/-}$, 3 experiments, n=18 oocytes for *Fmn2*$^{+/-}$ + NZ, 2 experiments, n=25 oocytes for *Fmn2*$^{-/-}$, 3 experiments and n=15 for *Fmn2*$^{-/-}$ + NZ, 2 experiments.

(D) Power spectrum of nuclear fluctuations over 5 min in the presence (dark color) or not (light color) of NZ: the squared moduli of the Fourier transforms of fluctuations (R-R) are plotted as a function of the mode for *Fmn2*$^{+/-}$ (green) and *Fmn2*$^{-/-}$ (red) nuclei. For *Fmn2*$^{-/-}$, the region of the large invagination was excluded from the measurements. Data are fitted to the function 1 / ($\bar{\sigma} n^2 + \bar{\kappa} n^4$) + Yinf according to the Helfrich model.

Table 1. Physical Parameters of the Helfrich Model

	Fmn2$^{+/-}$	*Fmn2*$^{+/-}$ + NZ	*Fmn2*$^{+/-}$ + CCD	*Fmn2*$^{-/-}$	*Fmn2*$^{-/-}$ + NZ
$l_c = R\sqrt{\bar{\kappa}/\bar{\sigma}}$	0.4	0.36	0.24	0.29	0.18
T_{cyto}/T_{ref} (the Effective Temperature T_{ref} of *Fmn2*$^{+/-}$ Is Taken as Reference	1	1.9	0.2	0.2	0.14
Yinf	2.068E-05	3.083E-05	2.811E-05	2.751E-05	1.840E-05

Results from fitting the Helfrich model.

Nuclear Envelope Fluctuations Correlate with Chromatin Motion

We reasoned that the cytoplasmic activity at steady state, inducing nuclear envelope fluctuations, could potentially be transmitted to the chromatin inside the nucleus, as previously observed in *Drosophila* embryos (Hampoelz et al., 2011). On physical grounds, the cytoplasm-based active fluctuations of the nuclear envelope exert fluctuating forces on the nuclear fluid and, therefore, on chromatin. We could thus expect chromatin to be subjected to an active temperature, induced by cytoplasmic activity and transduced by the nuclear envelope. Assuming that the nucleoplasm behaves as a viscous fluid, a simple physical model (see model in STAR Methods) predicts that the diffusion coefficient of a given tracer particle in the nucleus can be written $D = k_B(T + \alpha T_a)/\lambda$, where λ is a friction coefficient, T_a models the active fluctuations of the cytoskeletal meshwork introduced above, and α<1 is a numerical constant that accounts for the dampening of these active forces in the nucleus. In this picture, the chromatin experiences an effective temperature in the nucleoplasm, $T_{nuc} = T + \alpha T_a$, which actually depends on cytoplasmic activity.

To test the above model of cytoplasm-to-chromatin force transmission, we followed chromatin motion at high temporal resolution. Chromatin in control nuclei was more mobile and nucleoli explored more space when compared to *Fmn2*$^{-/-}$ or CCD-treated oocytes (Figures 4A and 4B; Videos S6 and S7), in agreement with a higher effective temperature in controls. The mean square displacement (MSD) (measuring the space explored by the unit of time) of the nucleolus increased linearly with time, characteristic of a sub-diffusive motion (Brangwynne et al., 2009), and arguing for the viscous fluid property of the nucleoplasm (Figure 4C). The fit of the MSD curves showed that the diffusion coefficient of the nucleolus was 3 times larger in control *Fmn2*$^{+/-}$ than in *Fmn2*$^{-/-}$ and 2.25 higher than in CCD-treated controls, suggesting that nucleolus movement depended on cytoplasmic F-actin (Figure 4C). Consistent with our physical model, the presented data suggested an effective temperature in the nucleoplasm, T_{nuc}, 3 times larger in controls versus *Fmn2*$^{-/-}$. It is noteworthy that the effective temperature, T_{nuc}, experienced by the chromatin is smaller than the effective temperature experienced by the nuclear envelope T_{cyto}. This could be due to the dampening of active forces within the nucleus.

The data suggested that the intrinsic properties of nuclei are comparable between controls and *Fmn2*$^{-/-}$ oocytes. To test whether chromatin motion depended mostly on external forces from the cytoplasm and not on intra-nuclear viscosity differences, we performed intra-nuclear FRAP experiments. For this, we used our nucleo-plasmic probe (Azoury et al., 2011), which diffuses independently of chromatin (Dumont et al., 2007b). Fluorescence recovery was identical in control *Fmn2*$^{+/-}$ and *Fmn2*$^{-/-}$nuclei, in support of similar intrinsic nucleo-plasmic properties in both conditions (Figures S3A and S3B).

Interestingly, the correlation between nuclear envelope fluctuations and chromatin motion was also observed with treatment of oocytes with NZ. Treatment of control *Fmn2*$^{+/-}$ oocytes with NZ increased nuclear envelope fluctuations (Figure 3C), increased about 2-fold the cytoplasmic effective temperature T_{cyto} (Table 1), and increased 1.6-fold chromatin motion (Figure 4D). Altogether, our results suggested that forces from the cytoskeleton generate a cytoplasmic activity which promotes nuclear envelope fluctuations associated to chromatin motion.

Gene Expression Is Modified in *Fmn2*$^{-/-}$ Oocytes

We then sought to test whether the newly found force transmission into the nucleus could affect chromosomal activity. To address this, we first reassessed the transcriptional status in control fully grown oocytes. We unexpectedly yet consistently detected foci of EU incorporation, which permits to detect RNA synthesis, in competent fully grown oocytes indicating transcriptional activity that was 5-fold less important than in smaller growing incompetent oocytes (Figures S4A and S4B). We then assessed if cytoplasmic activity dynamically shaping the nucleus and putting the chromatin in motion could affect gene expression by comparing the transcriptome of *Fmn2*$^{+/-}$ with *Fmn2*$^{-/-}$ oocytes using RNA-seq (Figure 5A). We found 256 genes significantly (p-adj < 0.05) misregulated in *Fmn2*$^{-/-}$ oocytes, most of which were downregulated (244) while only 12 genes were upregulated (Table S1). The large majority of misregulated genes were protein coding (Figure 5B), ten of which were validated by RT-qPCR (Figure 5C and Table 2). The population of misregulated genes was distributed on all chromosomes (Figure 5D). Relative to inherent chromosomal features, the amount of misregulated genes correlated positively with estimated physical sizes of chromosomes but not with total gene number per chromosome (Figures 5E and 5F). Despite the intrinsic size differences characterizing chromosomes, the loci of misregulated genes were still physically spread out along all chromosomes with comparable intra-chromosomal distributions of intergenic distances (Figure 5G). When compared to A/B compartments and lamin-associated domains (LADs) of ES cells (Bonev et al., 2017; Peric-Hupkes et al., 2010), the large majority of misregulated genes localized to A compartments (70%; Figure S5) and constitutive inter-LADs (75%; Figure S5) suggesting that these genes were in active chromatin domains. Altogether, the descriptive analyses of the RNA-seq suggest a global modulation of gene expression in *Fmn2*$^{-/-}$ oocytes. Together with the imaging analyses, the data argue

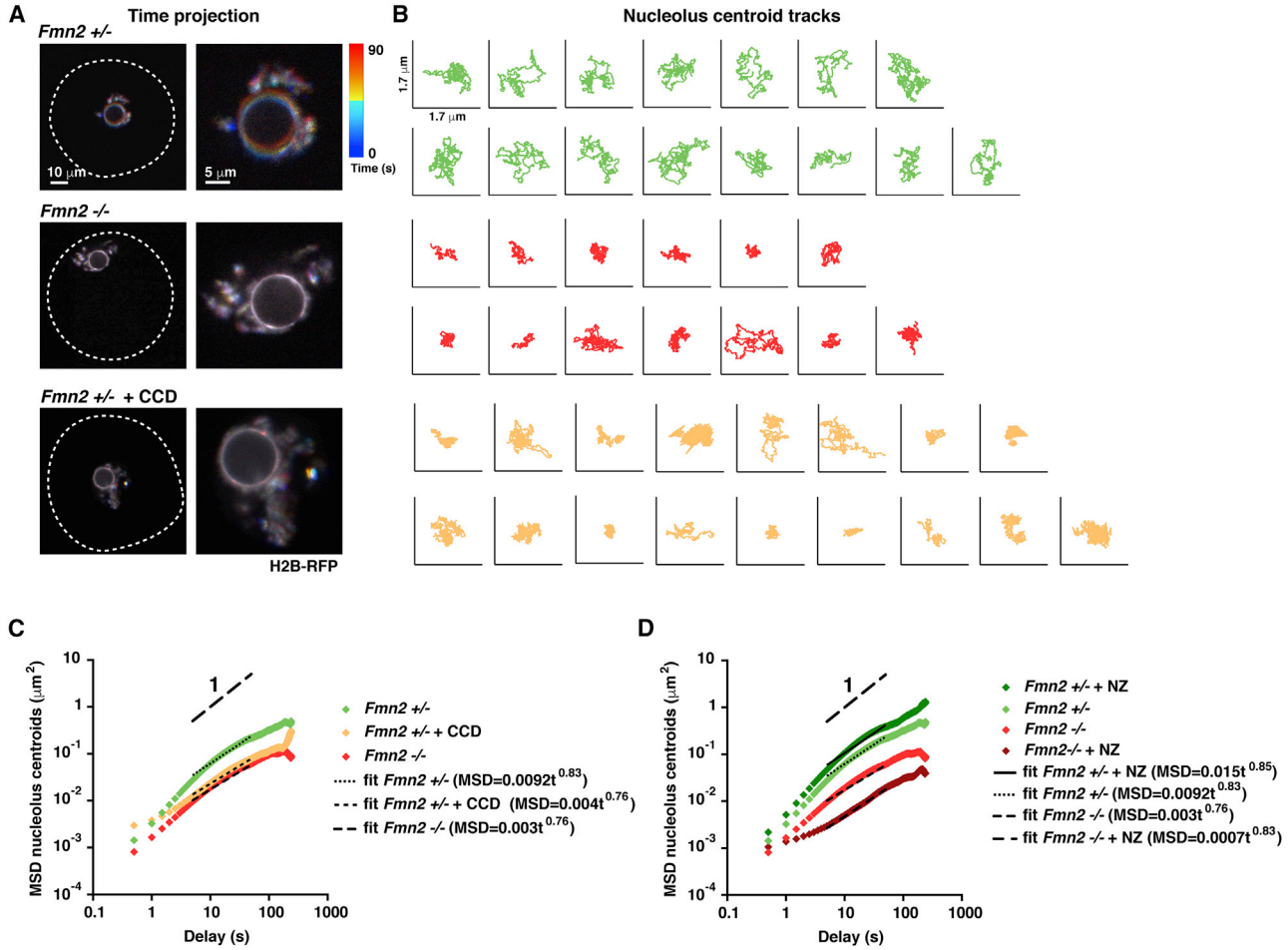

Figure 4. Nuclear Envelope Fluctuations Mediate Chromatin Motion

(A) Chromatin motion in oocytes with higher (*Fmn2*$^{+/-}$) or lower (*Fmn2*$^{-/-}$ and *Fmn2*$^{+/-}$ + CDD) nuclear envelope fluctuations. Left: One movie colored time-projection on 10 time points (90 sec) of a *Fmn2*$^{+/-}$ (top), a *Fmn2*$^{-/-}$ (middle), or a *Fmn2*$^{+/-}$ + CDD (bottom)-treated oocyte expressing H2B-RFP. Blue first timepoint, red last timepoint. The white dotted line represents the outline of the oocyte. Scale bar is 10 μm. right: Zoom of the chromatin area from the oocyte presented on the left panels. Scale bar is 5 μm.

(B) The nucleolus explores more space in *Fmn2*$^{+/-}$ versus *Fmn2*$^{-/-}$ or *Fmn2*$^{+/-}$ + CDD oocytes. Individual nucleolus centroid tracks from *Fmn2*$^{+/-}$ (top green), *Fmn2*$^{-/-}$ (middle red), *Fmn2*$^{-/-}$ (bottom orange) oocytes. Total duration of the tracking is 5 min.

(C) Oocytes with higher nuclear envelope fluctuations display more important chromatin motion. Mean MSD plot of nucleoli centroids in *Fmn2*$^{+/-}$ (green), *Fmn2*$^{-/-}$ (red) and *Fmn2*$^{+/-}$ + CCD oocytes (orange). Approximate power-law slope of 1 is indicated. n=29 oocytes for *Fmn2*$^{+/-}$, 3 experiments, n=24 oocytes for *Fmn2*$^{-/-}$, 3 experiments and n=16 for *Fmn2*$^{+/-}$ + CCD, one experiment

(D) Oocytes with higher nuclear envelope fluctuations display more important chromatin motion. Mean MSD plot of nucleoli centroids from *Fmn2*$^{+/-}$ + NZ (dark green), *Fmn2*$^{+/-}$ (green), *Fmn2*$^{-/-}$ (red) and *Fmn2*$^{+/-}$ + NZ oocytes (dark red). n=29 oocytes for *Fmn2*$^{+/-}$, 3 experiments, n=24 oocytes for *Fmn2*$^{-/-}$, 3 experiments, n=16 for *Fmn2*$^{+/-}$ + NZ, 2 experiments and n=13 for *Fmn2*$^{-/-}$ + NZ, 2 experiments.

for a link between cytoplasmic activity, nuclear architecture, and gene expression defects in oocytes.

Formin 2 Rescues Gene Expression in *Fmn2*$^{-/-}$ Oocytes

To assess if gene expression could be rescued by restoring F-actin and cytoplasmic activity in Formin 2-mutant oocytes, we performed RT-qPCR on Formin 2-injected *Fmn2*$^{-/-}$ oocytes. Full-length Formin 2 and the FH1-FH2 domain rescued two genes out of the four tested from *Fmn2*$^{-/-}$ oocytes (Figure S4C, left and middle panels), while the N-terminal construct, that does not nucleate actin, did not rescue any of the four genes tested (Figure S4C, right panel). The gene expression rescue was probably due to an effect on transcription since it was abolished by co-treating oocytes with α-amanitin, an RNA polymerase II inhibitor, during the nucleus repositioning assay (Almonacid et al., 2015) (Figure S4D). Then, to test a potential role for nuclear actin monomers (G-actin) in transcription (for a review Miyamoto and Gurdon, 2013), we compared nuclear actin monomer levels using a known G-actin sensor, RPEL1-GFP-NLS (Belin et al., 2013). We confirmed the probe's sensitivity to G-actin using CCD treatment, known to increase cellular actin monomer levels (Figures S6A and S6B). However, we did not find any differences between control *Fmn2*$^{+/-}$ and *Fmn2*$^{-/-}$ nuclei (Figures S6A and S6B), suggesting that changes in nuclear G-actin levels are not responsible for transcriptional gene expression changes found in Formin 2-mutant oocytes. Similarly, using another nuclear

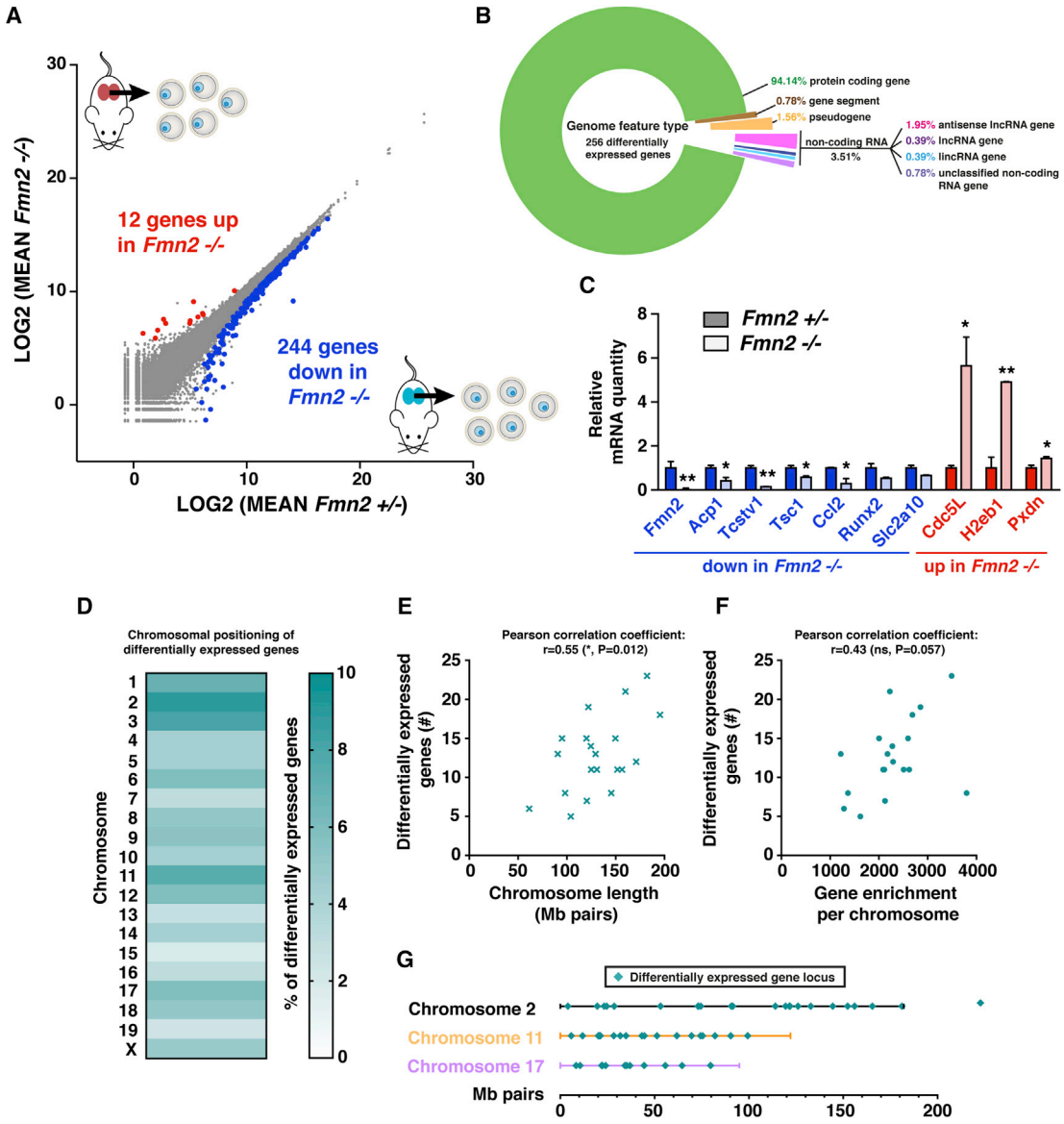

Figure 5. Genomic Distribution of Differentially Expressed Genes in *Fmn2*$^{-/-}$ Oocytes

(A) Differential gene expression in *Fmn2*$^{-/-}$ Prophase I-arrested oocytes. Differential transcriptomic analysis of *Fmn2*$^{+/-}$ versus *Fmn2*$^{-/-}$ fully grown oocytes performed by RNA-seq. Among the 23,474 detected transcripts, 244 are significantly downregulated and 12 upregulated in *Fmn2*$^{-/-}$ oocytes (adjusted p value p-adj < 0.05). For each condition *Fmn2*$^{+/-}$ and *Fmn2*$^{-/-}$, 2 biological replicates of 50 oocytes each and 3 technical replicates.

(B) Parts of whole donut graph representing the portions of genome feature types of differentially expressed genes.

(C) Confirmation of the transcriptomics analysis performed in A by RT-qPCR on a panel of 7 downregulated and 3 upregulated genes selected from their adjusted p value and $\log_2$ fold change. Mean of the normalized ratios of transcript levels between *Fmn2*$^{+/-}$ and *Fmn2*$^{-/-}$. Error bars represent normalized SEM. Normalized mean and SEM for *Fmn2*$^{+/-}$ are 1 ± 0.29 (Fmn2), 1 ± 0.13 (Acp1), 1 ± 0.11 (Tcstv1), 1 ± 0.11 (Tsc1), 1 ± 0.027 (Ccl2), 1 ± 0.2 (Runx2), 1 ± 0.12 (Slc2a10), 1 ± 0.11 (Cdc5L), 1 ± 0.49 (H2eb1) and 1 ± 0.13 (Pxdn). Normalized mean and SEM for *Fmn2*$^{-/-}$ are 0.065 ± 0.02 (Fmn2), 0.41 ± 0.15 (Acp1), 0.15 ± 0.006 (Tcstv1), 0.58 ± 0.068 (Tsc1), 0.3 ± 0.23 (Ccl2), 0.54 ± 0.036 (Runx2), 0.66 ± 0.021 (Slc2a10), 5.64 ± 1.3 (Cdc5L), 4.9 ± 0.016 (H2eb1) and 1.44 ± 0.08 (Pxdn). p values for student t test are 0.01 for Fmn2, 0.043 for Acp1, 0.0014 for Tcstv1, 0.034 for Tsc1, 0.022 for Ccl2, 0.084 for Runx2, 0.051 for Slc2a10, 0.012 for Cdc5L, 0.0013 for H2eb1, and 0.048 for Pxdn. 3 independent experiments, n=35 oocytes each for Acp1, Tcstv1, Tsc1, Runx2, Slc2a10, H2eb1, and Pxdn, and 4 experiments, n=35 oocytes each for Fmn2, Ccl2, and Cdc5L.

(D) Percentage heatmap showing the chromosomal origin of 256 differentially expressed genes in *Fmn2*$^{-/-}$ oocytes (p-adj < 0.05).

(E and F) Distribution of absolute numbers of differentially expressed genes per chromosome relative to (E) estimated individual mouse chromosome lengths in megabase pairs or (F) relative to individual mouse chromosome gene enrichment.

(G) Representative spreading of differentially expressed gene loci along a selection of chromosomes of various lengths.

Table 2. List of Genes, Confirmed by RT-qPCR, for the Transcriptomic Analysis of *Fmn2*$^{+/-}$ versus *Fmn2*$^{-/-}$ Oocytes

Gene	Function
Downregulated	
Fmn2	Actin nucleator
Acp1	Tyrosine phosphatase
Tcstv1	Zygotic genome activated
Tsc1	Wnt/β-catenin pathway
Ccl2	Chemotactic activator
Runx2	Formation of the dorso-ventral axis
Slc2a10	Glucose transporter
Upregulated	
Cdc5L	Splicing factor
H2eb1	MHC component
Pxdn	Peroxidase activity

Each gene is displayed with its function.

actin probe (nAC-GFP; Baarlink et al., 2017; Plessner et al., 2015), we also could not detect any differences in nuclear G-actin levels between control *Fmn2*$^{+/-}$ and *Fmn2*$^{-/-}$ nuclei (Figures S6C and S6D). These two results argue against a contribution of nuclear actin in the process we are studying here.

Thus, despite the previously described global shut down of transcription at the end of oocyte growth (Bouniol-Baly et al., 1999; De La Fuente and Eppig, 2001; Worrad et al., 1994), some loci are still active in fully grown oocytes prior to meiosis resumption. Our data indicate that cytoplasmic activity induced by microfilaments is transmitted to the chromatin via nuclear envelope fluctuations, regulating nucleus shape, and gene expression. If this is true, decreasing or increasing cytoplasmic activity should modify gene expression.

To test if modulations of cytoplasmic activity and thus strength of nuclear envelope fluctuations as well as nucleus shape indeed impact gene expression, we treated oocytes with either CCD or NZ, on two highly oppositely misregulated genes, Tcstv1 and Cdc5L. We could mimic the increase in Cdc5L levels observed in *Fmn2*$^{-/-}$ (Figure 5C) by treating controls with CCD (Figure S4E). NZ treatment had no effect on Tcstv1 and Cdc5L expression in *Fmn2*$^{+/-}$ oocytes (data not shown). Maybe the amplitude of the impact of NZ on chromatin motion in controls (1.6-fold more motion) was not sufficient to modulate gene expression (Figure 4D). However, NZ treatment affected their expression in *Fmn2*$^{-/-}$ oocytes. Their expression was inverted with respect to the one observed in *Fmn2*$^{+/-}$ versus *Fmn2*$^{-/-}$ oocytes (Figures 5C and S4F). Our results suggest that nuclear shape and nuclear envelope fluctuations can regulate the expression of at least some genes in oocytes lacking F-actin.

DISCUSSION

The transmission of external forces to the nucleus, known as mechano-transduction, has a far-reaching impact on cells (Graham and Burridge, 2016). Much has been learned on how forces from the cell surroundings modulate intracellular geometry, particularly how cytoskeletal elements transduce extracellular forces to organelles or to the mitotic spindle (Fink et al., 2011; Kunda et al., 2008; Théry et al., 2005, 2006, 2007). In adherent cells for instance, mechanical forces of environmental origin and artificial forces applied to integrins are transduced to the nucleus whose morphology is consequently impacted (Maniotis et al., 1997). Magnetic twisting cytometry can also induce the transcriptional upregulation of a multi-copy insertion of a bacterial artificial chromosome (BAC) in cultured cells via integrin-mediated local shear stress (Tajik et al., 2016). In mouse oocytes, Formin 2 is mostly known for being a straight F-actin nucleator required for chromosome positioning (Almonacid et al., 2015; Azoury et al., 2008, 2011; Chaigne et al., 2013; Dumont et al., 2007a; Leader et al., 2002; Pfender et al., 2011; Schuh, 2011; Schuh and Ellenberg, 2008). Bypassing this canonical function, Formin 2's involvement in chromatin dynamics and regulation of gene expression is highlighted by our study. Using a combination of knockout and drug treatments, we present evidence that Fmn2-assembled microfilaments in the cytoplasm exert non-thermal fluctuations of the nuclear envelope, subsequently enhancing chromatin diffusion, in absence of any modulation of the nuclear actin pool. The Fmn2-dependent forces impact external nuclear shape, internal architecture, and chromatin motion. Moreover, our rescue experiments show that, in a physiological context, the upregulation of endogenous gene transcription can be triggered via actin-based nucleus motion in mouse oocytes. Based on α-amanitin experiments, this phenomenon probably functions via endogenous transcriptional responses of the oocyte. We can detect a signature of a subset of genes up and downregulated in *Fmn2*$^{-/-}$ oocytes, or after treatment with specific F-actin and microtubule depolymerizing drugs, that potentially respond to mechano-transduction.

All oocytes undergo a massive transcriptional silencing, and it is only after fertilization, at various stages depending on the species, that zygotic transcription will be turned on (Patterton and Wolffe, 1996). Recent studies provided evidence that the quality of the oocyte maternal transcriptome controls the capacity to switch on zygotic genome activation after fertilization (Ancelin et al., 2016; Posfai et al., 2012; Wasson et al., 2016). We show that few loci are still transcriptionally active at the end of oocyte growth in the mouse. Together with findings in *Drosophila* oocytes (Mahowald and Tiefert, 1970; Navarro-Costa et al., 2016), our data argue against the commonly accepted dogma of full transcriptional shut down at the end of the Prophase I arrest. We show that the presence of actin filaments which drives nucleus centering is associated with misregulation of specific genes at active loci distributed along the whole genome. Importantly, an off-center nucleus correlates with a poor outcome for mouse and human oocyte development (Brunet and Maro, 2007; Levi et al., 2013). F-actin, which centers the nucleus, can also modulate the amount of maternal transcripts and hence the developmental potential of the female gamete.

It has been shown very recently that prophase I mouse oocytes do not contain detectable lamin-associated domains (LADs) and that LADs are formed *de novo* during early embryogenesis (Borsos et al., 2019). We could speculate that the F-actin-dependent mechanism we describe participates in the elimination of LADs at the end of oogenesis by favoring the equilibrium of forces around the nucleus. In its absence

(in *Fmn2*$^{-/-}$ or CDD-treated oocytes), microtubules nucleated from the major aMTOC penetrate the nucleus, producing an invagination which perturbs internal chromatin contacts, inducing mis-regulation at specific loci distributed on all chromosomes.

To conclude, this study highlights an original model of mechano-transduction that could be extended to other isolated models, such as early embryos, where the cell produces its own internal forces affecting nuclear shape, state of chromatin condensation, and gene expression.

STAR METHODS

Detailed methods are provided in the online version of this paper and include the following:

- KEY RESOURCES TABLE
- LEAD CONTACT AND MATERIALS AVAILABILITY
- EXPERIMENTAL MODEL AND SUBJECT DETAILS
- METHOD DETAILS
  - Oocyte Collection, Culture, and Microinjection
  - Drug Treatments
  - Oocyte RNA Extraction, cDNA Synthesis, and Quantitative PCR
  - RNA Extraction for RNA-Seq
  - cDNA Libraries and RNA-Seq
  - Bioinformatics Analysis
  - Gene Ontology Analysis
  - Live Imaging
  - Immunofluorescence
  - Image Analysis
  - Computational 3D Imaging
  - Bio-Physical Model
  - Non-linear Fitting of Fourier Transforms
- QUANTIFICATION AND STATISTICAL ANALYSIS
- DATA AND CODE AVAILABILITY

SUPPLEMENTAL INFORMATION

Supplemental Information can be found online at https://doi.org/10.1016/j.devcel.2019.09.010.

ACKNOWLEDGMENTS

We thank Cécile Sykes (Curie Institute) and Marie-Emilie Terret (CIRB) for critical reading of the manuscript. We thank Isabelle Queguiner for the purification of mRNAs from oocytes. Library preparation and Illumina sequencing were performed at the Ecole Normale Supérieure Genomic Platform (IBENS, Paris, France). We thank Léa Bellenger, Michel Raymond, and Christophe Antoniewski from the "ARTbio bioinformatics platform" at the IBPS for their services and discussion. We thank Hugo Brandao (Harvard University) for sharing A/B compartments scores. We thank Dyche Mullins (UCSF) for the RPEL1-GFP-NLS construct. The work at IBENS Genomic Platform was supported by the France Génomique national infrastructure, funded as part of the "Investissements d'Avenir" program managed by the Agence Nationale de la Recherche (reference: ANR-10-INBS-09). A.A.J. is funded by the Fondation ARC (grant reference: PDF2017050561). This work was supported by grants from the Fondation pour la Recherche Médicale (FRM Label to M.H.V., DEQ20150331758), from the ANR-DIVACEN (to M.H.V. and Renata Basto, Curie Institute, N°14-CE11), by a PSL "Aux Frontière des Labex" grant (MYOOCYTE, M.H.V. as coordinator) and from the Labex Memolife (to M.H.V. and A.G.). This work has received support under the program "Investissements d'Avenir" launched by the French Government and implemented by the ANR, with the references ANR-10-LABX-54 MEMO LIFE and ANR-11-IDEX-0001-02 PSL* Research University.

AUTHOR CONTRIBUTIONS

M.A. and M.H.V. conceived and supervised the project. M.A. performed most experiments. M.A. and M.H.V. analyzed most experiments. A.O. and A.G. conceived and did the 3D computational imaging approach. A.G. did the measure of correlation between nuclear outline and chromatin motion. T.P. assisted with FRAP experiments. A.A.J. directed the analysis of the RNA-seq data in collaboration with the IBPS bioinformatics facility (ARTbio). S.E.H. performed and analyzed the RT-qPCRs. F.C. and S.L. did the cDNA libraries and performed the RNA-seq. P.M. did the plugins to analyze nuclear envelope fluctuations and nucleolus tracking. C.K. did the fit for Fourier Transform analysis. R.V. designed the mathematical model. M.A., A.A.J., and M.H.V. wrote the manuscript, which was seen and corrected by all authors.

DECLARATION OF INTERESTS

The authors declare no competing interests.

Received: January 23, 2019
Revised: June 14, 2019
Accepted: September 13, 2019
Published: October 10, 2019

REFERENCES

Achanta, R., Shaji, A., Smith, K., Lucchi, A., Fua, P., and Süsstrunk, S. (2012). SLIC superpixels compared to state-of-the-art superpixel methods. IEEE Trans. Pattern Anal. Mach. Intell. *34*, 2274–2282.

Almonacid, M., Ahmed, W.W., Bussonnier, M., Mailly, P., Betz, T., Voituriez, R., Gov, N.S., and Verlhac, M.H. (2015). Active diffusion positions the nucleus in mouse oocytes. Nat. Cell Biol. *17*, 470–479.

Ancelin, K., Syx, L., Borensztein, M., Ranisavljevic, N., Vassilev, I., Briseño-Roa, L., Liu, T., Metzger, E., Servant, N., Barillot, E., et al. (2016). Maternal LSD1/KDM1A is an essential regulator of chromatin and transcription landscapes during zygotic genome activation. Elife *5*, e08851.

Arasan, S., Hasiloglu, A.S., and Akbulut, S. (2010). Shape properties of natural and crushed aggregate using image analysis. Int. J. Civ. Struct. Eng. *1*, 221–233.

Azoury, J., Lee, K.W., Georget, V., Rassinier, P., Leader, B., and Verlhac, M.H. (2008). Spindle positioning in mouse oocytes relies on a dynamic meshwork of actin filaments. Curr. Biol. *18*, 1514–1519.

Azoury, J., Lee, K.W., Georget, V., Hikal, P., and Verlhac, M.H. (2011). Symmetry breaking in mouse oocytes requires transient F-actin meshwork destabilization. Development *138*, 2903–2908.

Baarlink, C., Plessner, M., Sherrard, A., Morita, K., Misu, S., Virant, D., Kleinschnitz, E.M., Harniman, R., Alibhai, D., Baumeister, S., et al. (2017). A transient pool of nuclear F-actin at mitotic exit controls chromatin organization. Nat. Cell Biol. *19*, 1389–1399.

Belin, B.J., Cimini, B.A., Blackburn, E.H., and Mullins, R.D. (2013). Visualization of actin filaments and monomers in somatic cell nuclei. Mol. Biol. Cell *24*, 982–994.

Bonev, B., Mendelson Cohen, N., Szabo, Q., Fritsch, L., Papadopoulos, G.L., Lubling, Y., Xu, X., Lv, X., Hugnot, J.P., Tanay, A., et al. (2017). Multiscale 3D genome rewiring during mouse neural development. Cell *171*, 557–572.

Borsos, M., Perricone, S.M., Schauer, T., Pontabry, J., de Luca, K.L., de Vries, S.S., Ruiz-Morales, E.R., Torres-Padilla, M.E., and Kind, J. (2019). Genome-lamina interactions are established de novo in the early mouse embryo. Nature *569*, 729–733.

Bouniol-Baly, C., Hamraoui, L., Guibert, J., Beaujean, N., Szöllösi, M.S., and Debey, P. (1999). Differential transcriptional activity associated with chromatin configuration in fully grown mouse germinal vesicle oocytes. Biol. Reprod. *60*, 580–587.

Brangwynne, C.P., Koenderink, G.H., MacKintosh, F.C., and Weitz, D.A. (2009). Intracellular transport by active diffusion. Trends Cell Biol. *19*, 423–427.

Brunet, S., and Maro, B. (2007). Germinal vesicle position and meiotic maturation in mouse oocyte. Reproduction *133*, 1069–1072.

Chaigne, A., Campillo, C., Gov, N.S., Voituriez, R., Azoury, J., Umaña-Diaz, C., Almonacid, M., Queguiner, I., Nassoy, P., Sykes, C., et al. (2013). A soft cortex is essential for asymmetric spindle positioning in mouse oocytes. Nat. Cell Biol. *15*, 958–966.

De La Fuente, R., and Eppig, J.J. (2001). Transcriptional activity of the mouse oocyte genome: companion granulosa cells modulate transcription and chromatin remodeling. Dev. Biol. *229*, 224–236.

Deviri, D., Pfeifer, C.R., Dooling, L.J., Ivanovska, I.L., Discher, D.E., and Safran, S.A. (2019). Scaling laws indicate distinct nucleation mechanisms of holes in the nuclear lamina. Nat. Phys. *15*, 823–829.

Dobin, A., Davis, C.A., Schlesinger, F., Drenkow, J., Zaleski, C., Jha, S., Batut, P., Chaisson, M., and Gingeras, T.R. (2013). STAR: ultrafast universal RNA-seq aligner. Bioinformatics *29*, 15–21.

Dumont, J., Million, K., Sunderland, K., Rassinier, P., Lim, H., Leader, B., and Verlhac, M.H. (2007a). Formin-2 is required for spindle migration and for the late steps of cytokinesis in mouse oocytes. Dev. Biol. *301*, 254–265.

Dumont, J., Petri, S., Pellegrin, F., Terret, M.E., Bohnsack, M.T., Rassinier, P., Georget, V., Kalab, P., Gruss, O.J., and Verlhac, M.H. (2007b). A centriole- and RanGTP-independent spindle assembly pathway in meiosis I of vertebrate oocytes. J. Cell Biol. *176*, 295–305.

van Eeden, F., and St Johnston, D. (1999). The polarisation of the anterior-posterior and dorsal-ventral axes during *Drosophila* oogenesis. Curr. Opin. Genet. Dev. *9*, 396–404.

Fink, J., Carpi, N., Betz, T., Bétard, A., Chebah, M., Azioune, A., Bornens, M., Sykes, C., Fetler, L., Cuvelier, D., et al. (2011). External forces control mitotic spindle positioning. Nat. Cell Biol. *13*, 771–778.

FitzHarris, G., Marangos, P., and Carroll, J. (2007). Changes in endoplasmic reticulum structure during mouse oocyte maturation are controlled by the cytoskeleton and cytoplasmic dynein. Dev. Biol. *305*, 133–144.

Graham, D.M., and Burridge, K. (2016). Mechanotransduction and nuclear function. Curr. Opin. Cell Biol. *40*, 98–105.

Gundersen, G.G., and Worman, H.J. (2013). Nuclear positioning. Cell *152*, 1376–1389.

Halet, G., and Carroll, J. (2007). Rac activity is polarized and regulates meiotic spindle stability and anchoring in mammalian oocytes. Dev. Cell *12*, 309–317.

Hampoelz, B., Azou-Gros, Y., Fabre, R., Markova, O., Puech, P.H., and Lecuit, T. (2011). Microtubule-induced nuclear envelope fluctuations control chromatin dynamics in *Drosophila* embryos. Development *138*, 3377–3386.

Kovar, D.R. (2006). Molecular details of formin-mediated actin assembly. Curr. Opin. Cell Biol. *18*, 11–17.

Kubo, R. (1966). The fluctuation-dissipation theorem. Rep. Prog. Phys. *29*, 255–284.

Kunda, P., Pelling, A.E., Liu, T., and Baum, B. (2008). Moesin controls cortical rigidity, cell rounding, and spindle morphogenesis during mitosis. Curr. Biol. *18*, 91–101.

Leader, B., Lim, H., Carabatsos, M.J., Harrington, A., Ecsedy, J., Pellman, D., Maas, R., and Leder, P. (2002). Formin-2, polyploidy, hypofertility and positioning of the meiotic spindle in mouse oocytes. Nat. Cell Biol. *4*, 921–928.

Levi, M., Ghetler, Y., Shulman, A., and Shalgi, R. (2013). Morphological and molecular markers are correlated with maturation-competence of human oocytes. Hum. Reprod. *28*, 2482–2489.

Love, M.I., Huber, W., and Anders, S. (2014). Moderated estimation of fold change and dispersion for RNA-seq data with DESeq2. Genome Biol. *15*, 550.

Luksza, M., Queguigner, I., Verlhac, M.H., and Brunet, S. (2013). Rebuilding MTOCs upon centriole loss during mouse oogenesis. Dev. Biol. *382*, 48–56.

Mahowald, A.P., and Tiefert, M. (1970). Fine structural changes in the *Drosophila* oocyte nucleus during a short period of RNA synthesis: an autoradiographic and ultrastructural study of RNA synthesis in the oocyte nucleus of *Drosophila*. Wilhelm Roux Arch. Entwickl. Mech. Org. *165*, 8–25.

Marthiens, V., Rujano, M.A., Pennetier, C., Tessier, S., Paul-Gilloteaux, P., and Basto, R. (2013). Centrosome amplification causes microcephaly. Nat. Cell Biol. *15*, 731–740.

Manil-Ségalen, M., Łuksza, M., Kanaan, J., Marthiens, V., Lane, S.I.R., Jones, K.T., Terret, M.E., Basto, R., and Verlhac, M.H. (2018). Chromosome structural anomalies due to aberrant spindle forces exerted at gene editing sites in meiosis. J. Cell Biol. *217*, 3416–3430.

Maniotis, A.J., Chen, C.S., and Ingber, D.E. (1997). Demonstration of mechanical connections between integrins, cytoskeletal filaments, and nucleoplasm that stabilize nuclear structure. Proc. Natl. Acad. Sci. USA *94*, 849–854.

Martinez, A.M., and Kak, A.C. (2001). PCA versus LDA. IEEE Trans. Pattern Anal. Machine Intell *23*, 228–233.

Miyamoto, K., and Gurdon, J.B. (2013). Transcriptional regulation and nuclear reprogramming: roles of nuclear actin and actin-binding proteins. Cell. Mol. Life Sci. *70*, 3289–3302.

Navarro-Costa, P., McCarthy, A., Prudêncio, P., Greer, C., Guilgur, L.G., Becker, J.D., Secombe, J., Rangan, P., and Martinho, R.G. (2016). Early programming of the oocyte epigenome temporally controls late prophase I transcription and chromatin remodeling. Nat. Commun. *7*, 12331.

Nelson, D.R., Piran, T., and Weinberg, S. (1989). Statistical Mechanics of Membranes and Surfaces (World Scientific).

Patterton, D., and Wolffe, A.P. (1996). Developmental roles for chromatin and chromosomal structure. Dev. Biol. *173*, 2–13.

Peric-Hupkes, D., Meuleman, W., Pagie, L., Bruggeman, S.W.M., Solovei, I., Brugman, W., Gräf, S., Flicek, P., Kerkhoven, R.M., van Lohuizen, M., et al. (2010). Molecular maps of the reorganization of genome-nuclear lamina interactions during differentiation. Mol. Cell *38*, 603–613.

Pfender, S., Kuznetsov, V., Pleiser, S., Kerkhoff, E., and Schuh, M. (2011). Spire-type actin nucleators cooperate with Formin-2 to drive asymmetric oocyte division. Curr. Biol. *21*, 955–960.

Plessner, M., Melak, M., Chinchilla, P., Baarlink, C., and Grosse, R. (2015). Nuclear F-actin formation and reorganization upon cell spreading. J. Biol. Chem. *290*, 11209–11216.

Posfai, E., Kunzmann, R., Brochard, V., Salvaing, J., Cabuy, E., Roloff, T.C., Liu, Z., Tardat, M., van Lohuizen, M., Vidal, M., et al. (2012). Polycomb function during oogenesis is required for mouse embryonic development. Genes Dev. *26*, 920–932.

Reis, A., Chang, H.Y., Levasseur, M., and Jones, K.T. (2006). APCcdh1 activity in mouse oocytes prevents entry into the first meiotic division. Nat. Cell Biol. *8*, 539–540.

Riechmann, V., and Ephrussi, A. (2001). Axis formation during *Drosophila* oogenesis. Curr. Opin. Genet. Dev. *11*, 374–383.

Roth, S. (2003). The origin of dorsoventral polarity in *Drosophila*. Philos. Trans. R. Soc. Lond., B, Biol. Sci. *358*, 1317–1329.

Roth, S., and Lynch, J.A. (2009). Symmetry breaking during *Drosophila* oogenesis. Cold Spring Harb. Perspect. Biol. *1*, a001891.

Schindelin, J., Arganda-Carreras, I., Frise, E., Kaynig, V., Longair, M., Pietzsch, T., Preibisch, S., Rueden, C., Saalfeld, S., Schmid, B., et al. (2012). Fiji: an open-source platform for biological-image analysis. Nat. Methods *9*, 676–682.

Schuh, M. (2011). An actin-dependent mechanism for long-range vesicle transport. Nat. Cell Biol. *13*, 1431–1436.

Schuh, M., and Ellenberg, J. (2008). A new model for asymmetric spindle positioning in mouse oocytes. Curr. Biol. *18*, 1986–1992.

Tajik, A., Zhang, Y., Wei, F., Sun, J., Jia, Q., Zhou, W., Singh, R., Khanna, N., Belmont, A.S., and Wang, N. (2016). Transcription upregulation via force-induced direct stretching of chromatin. Nat. Mater. *15*, 1287–1296.

Terret, M.E., Lefebvre, C., Djiane, A., Rassinier, P., Moreau, J., Maro, B., and Verlhac, M.H. (2003). DOC1R: a MAP kinase substrate that control microtubule organization of metaphase II mouse oocytes. Development *130*, 5169–5177.

Théry, M., Racine, V., Pépin, A., Piel, M., Chen, Y., Sibarita, J.B., and Bornens, M. (2005). The extracellular matrix guides the orientation of the cell division axis. Nat. Cell Biol. *7*, 947–953.

Théry, M., Racine, V., Piel, M., Pépin, A., Dimitrov, A., Chen, Y., Sibarita, J.B., and Bornens, M. (2006). Anisotropy of cell adhesive microenvironment governs cell internal organization and orientation of polarity. Proc. Natl. Acad. Sci. USA *103*, 19771–19776.

Théry, M., Jiménez-Dalmaroni, A., Racine, V., Bornens, M., and Jülicher, F. (2007). Experimental and theoretical study of mitotic spindle orientation. Nature *447*, 493–496.

Tsurumi, C., Hoffmann, S., Geley, S., Graeser, R., and Polanski, Z. (2004). The spindle assembly checkpoint is not essential for CSF arrest of mouse oocytes. J. Cell Biol. *167*, 1037–1050.

Verlhac, M.H., Lefebvre, C., Guillaud, P., Rassinier, P., and Maro, B. (2000). Asymmetric division in mouse oocytes: with or without Mos. Curr. Biol. *10*, 1303–1306.

Wasson, J.A., Simon, A.K., Myrick, D.A., Wolf, G., Driscoll, S., Pfaff, S.L., Macfarlan, T.S., and Katz, D.J. (2016). Maternally provided LSD1/KDM1A enables the maternal-to-zygotic transition and prevents defects that manifest postnatally. Elife *5*, e08848.

Worrad, D.M., Ram, P.T., and Schultz, R.M. (1994). Regulation of gene expression in the mouse oocyte and early preimplantation embryo: developmental changes in Sp1 and TATA box-binding protein, TBP. Development *120*, 2347–2357.

STAR METHODS

KEY RESOURCES TABLE

REAGENT or RESOURCE	SOURCE	IDENTIFIER
Antibodies		
Rabbit Monoclonal Anti-Lamin A Clone (EP4520-16)	Abcam	Cat# ab133256; RRID: AB_2813767
Chemicals, Peptides, and Recombinant Proteins		
Cytochalasin D	Thermofisher	Cat#PHZ1063; CAS: 22144-77-0
Alpha-Amanitin	Sigma	Cat#A2263; CAS: 23109-05-9
Nocodazole	Sigma	Cat#M1404; CAS: 31430-18-9
Critical Commercial Assays		
Click-IT RNA Alexa Fluor 488 Imaging Kit	Thermofisher	Cat#C10329
mMESSAGEmMACHINE SP6 Transcription Kit	Thermofisher	Cat#AM1340
mMESSAGEmMACHINE T3 Transcription Kit	Themofisher	Cat#AM1348
RNAqueous Micro Total RNA Isolation Kit	Thermofisher	Cat#AM1931
Superscript II Kit	Thermofisher	Cat#18064014
LightCycler 480 SYBR Green I Master	Roche	Cat#04707516001
IScript Reverse Transcription SuperMix	Bio-Rad (Hercules, California, United States of America)	Cat#1708840
SsoAdvanced Universal SYBR Green SuperMix	Bio-Rad	Cat#1725270
Ovation RNA-Seq System V2	NuGEN	Cat#7102
TruSeq RNA Sample Preparation Kit v2	Illumina	Cat#RS-122-2001
Deposited Data		
RNA-Seq Data	This paper	GEO : GSE103718
Experimental Models: Organisms/Strains		
Mouse : OF1	Charles River (Margate, UK)	612
Mouse : *Fmn2*$^{+/-}$ and *Fmn2*$^{-/-}$	Leader et al., 2002 and this study	N/A
Oligonucleotides		
Primers for qPCR, See Table S1		N/A
Recombinant DNA		
pCS2-Fmn2-Myc	Gift from Philip Leder and this study	N/A
pCS2-Fmn2-GFP	Gift from Philip Leder and this study	N/A
pCS2-Nter-GFP	This study	N/A
pCS2-FH1-FH2-GFP	This study	N/A
pRN3-YFP-Rango-CFP	Dumont et al., 2007b	N/A
pRN3-mCherry-Plk4	Marthiens et al., 2013 and this study	N/A
pRN3-H2B-RFP	Tsurumi et al., 2004	N/A
pCS2-nAC-GFP	Baarlink et al., 2017	N/A
pRN3-RPEL1-GFP-NLS3	Belin et al., 2013 and this study	N/A
Software and Algorithms		
STAR	Dobin et al., 2013	N/A
DESeq2	Love et al., 2014	N/A
Galaxy Versions 2.6.0b-1 and 2.11.39		https://usegalaxy.org/
GO Enrichment Analysis (PANTHER)		http://geneontology.org/
MetaMorph Version 7.7.9.0	Universal Imaging	N/A
Fiji	Schindelin et al., 2012	https://fiji.sc/
R Version 3.3.2		https://www.r-project.org/
MATLAB Version 2016a	MathWorks	N/A
Python 2.7 Version 0.11.3		https://www.python.org/

(*Continued on next page*)

Continued

REAGENT or RESOURCE	SOURCE	IDENTIFIER
Prism v 7.0	GraphPad	N/A
3D Computational Analysis of Nuclear Architecture	This study	https://github.com/biocompibens/Meiospin
Analysis of Nuclear Envelope Fluctuations and Tracking of the Nucleoli	This study	https://github.com/pmailly/Ovocyte_Nucleus_Analyze

LEAD CONTACT AND MATERIALS AVAILABILITY

Further information and requests for resources and reagents should be directed to and will be fulfilled by the Lead Contact, Marie-Hélène Verlhac (marie-helene.verlhac@college-de-france.fr). Plasmids and other reagents generated in the study will be available upon request. Plasmids generated in this study have not been deposited but are available in the lab. This study did not generate new mouse lines.

EXPERIMENTAL MODEL AND SUBJECT DETAILS

Oocytes were collected by mouth pipetting from shredded ovaries. The ovaries came from 11 week-old OF1 and 15 week-old Formin 2 (*Fmn2*$^{+/-}$ or *Fmn2*$^{-/-}$) knockout female mice (Leader et al., 2002). *Fmn2*$^{-/-}$ males were crossed with *Fmn2*$^{+/-}$ females to obtain both *Fmn2*$^{+/-}$ and *Fmn2*$^{-/-}$ female genotypes for experiments. Mice were housed in environmentally controlled rooms in the Animal Facility of the CIRB, Collège de France. All experiments with mice were performed with approval from the Animal Care and Use Committee of the CIRB, Collège de France and from the French Ministry of Agriculture (authorization N°75-1170). The use of genetically modified organisms has been granted by the DGRI (Direction Générale de la Recherche et de l'Innovation: GMO agreement number DUO-1783).

METHOD DETAILS

Oocyte Collection, Culture, and Microinjection

Plasmids and In Vitro *Transcription of RNAs*

We used the following constructs: pCS2-Fmn2-Myc and pCS2-Fmn2-GFP (gifts from Philip Leder with modifications on amino acids sequence S944→P, L946→P, V1040→M, L1142→P according to Formin 2 protein sequence NP_062318.2), pRN3-YFP-Rango-CFP (Dumont et al., 2007b), pRN3-mCherry-Plk4 (Manil-Ségalen et al., 2018), pRN3-H2B-RFP (Tsurumi et al., 2004) and pCS2-nAC-GFP (Baarlink et al., 2017; Plessner et al., 2015). pCS2-Nter-GFP was constructed by cloning the N-terminal domain of Formin 2 (amino acids 1 to 734) into pCS2-GFP. pCS2-FH1-FH2-GFP was constructed by cloning the N-myristoyl domain MGNQDGK of Formin 2 (amino acids 1 to 7) and linker GGSGGGSG connected to the FH1-FH2 domain (amino acids 734 to 1578) into pCS2-GFP. pRN3-RPEL1-GFP-NLS3 was cloned in a pEGFP-N1 backbone (gift from Dyche Mullins; Belin et al., 2013). *In vitro* synthesis of capped cRNAs was performed as previously described (Terret et al., 2003) using the SP6 (Thermofisher, Ref. AM1340) or T3 mMESSAGEmMACHINE (Thermofisher, Ref. AM1384) transcription kit. cRNAs for the nAC-GFP probe were used at 200 ng μL^{-1}. RNAs were centrifuged at 4°C during 45 min at 13,000 rpm before microinjection.

Drug Treatments

Cytochalasin D (Thermofisher, Ref. PHZ1063) was used on oocytes at 1 $\mu g\ mL^{-1}$. α-amanitin (Sigma, Ref. A2263) was used on oocytes at 75 $\mu g\ mL^{-1}$. Nocodazole (Sigma, Ref. M1404) was used on oocytes at 1 μM. For nuclear envelope fluctuations and H2B-RFP movies, Prophase I-arrested oocytes were previously incubated for 1 h 30 with Cytochalasin D (CCD) or for 2 h with Nocodazole (NZ). For RPEL1 experiments, Prophase I-arrested oocytes were previously incubated for 3 h with CCD. For RT-qPCR experiments following CCD or NZ treatment, oocytes were kept for 5 h in the drug before RNA extraction.

To block transcription, Prophase-I arrested oocytes were incubated for 1 h in 75 $\mu g\ mL^{-1}$ α-amanitin (Sigma Ref. A2263) before microinjection for rescue experiments and then for the whole duration of the nucleus centring process.

Oocyte RNA Extraction, cDNA Synthesis, and Quantitative PCR

Total RNA was extracted from freshly collected oocytes (25 oocytes per sample) using the RNAqueous Micro Total RNA Isolation Kit (Thermofisher, Ref. AM1931) following the manufacturer's instructions. RNA was eluted in 20 μl of elution buffer. For confirmation of the transcriptomic analysis of *Fmn2*$^{+/-}$ compared to *Fmn2*$^{-/-}$ (Figure 5C), rescue experiments (Figures S4C and S4D) and for CCD experiments (Figure S4E), we used the SuperScript II kit (Thermofisher, Ref. 18064014) following the manufacturer's instructions with random primers. The cDNA was then used for quantitative PCR using LightCycler 480 SYBR Green I Master (Roche, Ref. 04707516001) and LightCycler 480 (Roche) with the primer pairs listed at the end of this section. For NZ experiments (Figure S4F), iScript Reverse Transcription supermix (Bio-Rad, Ref. 1708840) was used following the manufacturer's instructions. The cDNA was then used for quantitative PCR using SsoAdvanced Universal SYBR Green supermix (Bio-Rad, Ref. 1725270) and CFX-96 (Bio-Rad). For confirmation of the transcriptomic analysis (Figure 5C), mRNA quantity was normalized to Beta-actin (Actb). Relative expression

levels were calculated using the 2-ΔΔC. Mean and SEM were both normalized relative to *Fmn2*$^{+/-}$. For rescue, CCD and NZ experiments (Figures S4C–S4F), mRNA quantity was normalized to Beta-actin (Actb). Relative expression levels were calculated using the 2-ΔΔC and normalized relative to non-injected or untreated oocytes in each experiment. For NZ treatment, relative expression levels were calculated using the 2-ΔΔC and normalized relative to *Fmn2*$^{+/-}$ oocytes. Then the mean and SEM of normalized expression levels were calculated.

Primers for qPCR

Oocytes were maintained in Prophase I in M2+BSA medium supplemented with 1 μM Milrinone (Reis et al., 2006). At this stage, they were microinjected with cRNAs using an Eppendorf Femtojet microinjector. Oocytes were kept a minimum amount of time in Prophase I to allow sufficient expression of the various probes. It was respectively between 1 and 2 h for YFP-Rango or H2B-RFP, 4 h for RPEL1-GFP-3NLS, 2h30 for nAC-GFP and 2h30 for FRAP experiments on YFP-Rango. The expression time was identical for all types of oocytes in the various settings. For rescue experiments, *Fmn2*$^{-/-}$ oocytes were kept in Prophase I for 8 h after microinjection of Fmn2, FH1-FH2 or Nter cRNAs. This duration ensured that most oocytes completed the nucleus centring process (which is about 5 h; Almonacid et al., 2015). For rescue experiments with Nter cRNAs, where the nucleus does not centre, oocytes were checked for Nter-GFP fluorescence. For detection of nascent transcripts, Prophase I arrested oocytes were incubated for 4 h with 100 μM of the nucleoside analog 5′-ethynyl uridine (EU) from the Click-IT RNA Alexa Fluor 488 Imaging kit (Thermofisher, Ref. C10329). All live culture and imaging were carried out under oil at 37°C.

Gene Name	Forward Primer Sequence	Reverse Primer Sequence
Acp1	AGAAAGGCCATGATGTCCCA	CCTCTCCCTTCCTCGGTTTT
Actb	GGCTGTATTCCCCTCCATCG	CCAGTTGGTAACAATGCCATGT
Ccl2	ACTCGGACTGTGATGCCTTA	TGGATCCACACCTTGCATTT
Cdc5l	TCAGCAGAGATACGCGGATT	AACCAGCAACTCGATCTCCT
Fmn2	TTTGACATGCCTGGGTTGTG	ACCAATCTTTTCCTGACAGAGTG
H2eb1	GGCTCAAGTCAACGGTGTTT	ATTCGGCTGTGGACCTACAA
Pxdn	TGGGAAAGCACACGAGTTTG	GGTGGTGTGAATGTCCCCTA
Runx2	GGAACAACAACAACAACAACAAC	ACGATCATGACCTGTGGCA
Tcstv1	CCCAGAGTACAAGGTGTTCTAATTC	CAAAAGGAGTATAGATCCCATTCGG
Tsc1	GGAAGGGAGAGGAGGACTTG	TGGTCCAGTCTCATGAAGGG

RNA Extraction for RNA-Seq

Fully grown Prophase I-arrested oocytes were selected following morphological criteria (size, zona thickness, perivitelline space). Total RNA was extracted from oocytes (freshly collected; 2 samples of *Fmn2*$^{+/-}$ and of *Fmn2*$^{-/-}$; 50 oocytes per sample) using the RNAqueous®-Micro Total RNA Isolation Kit (Thermofisher, Ref. AM1931). Oocytes were washed 3 times in PBS, resuspended in lysis buffer, freezed in liquid nitrogen and conserved at -80°C overnight. After unfreezing, RNA extraction was carried out following the manufacturer's instructions. RNA was eluted twice in 10 μl elution buffer. Samples were then treated with DNAse I.

cDNA Libraries and RNA-Seq

1 ng of total RNA was amplified and converted to cDNA using the Ovation RNA-Seq kit V2 (NuGEN, Ref. 7102). Following amplification, 1 μg of cDNA was fragmented to approximately 200 bps using Covaris S200. The remainder of the library preparation was done using 200 ng of cDNA following TruSeq RNA Sample Prep v2 kit (Illumina, Ref. RS-122-2001) from the End Repair step. Libraries were multiplexed by 4 on 1 flow cell lane. A 50 bp read sequencing was performed on a HiSeq 1500 device (Illumina). A mean of 17.3 ± 3.9 million passing Illumina quality filter reads was obtained for each of the 4 samples. For each biological sample, 3 technical replicates were done.

Bioinformatics Analysis

Raw reads passing Illumina quality filters were cleaned of adapters and mapped with STAR (Dobin et al., 2013) (Galaxy Version 2.6.0b-1). For each sample, between 4 and 15 million reads were mapped at a unique location on the *Mus musculus* genome (mm9 with Gencode mV1 annotation). Read counts per gene were also generated by STAR, and the DESeq2 package (Love et al., 2014) (Galaxy Version 2.11.39) was eventually used for differential expression analysis by the ARTbio bioinformatics platform. Differentially expressed genes with an adjusted p value (False Discovery Rate) threshold of 0.05 were selected for further analysis. Data on mouse chromosomes and genome features used for the descriptive analyses of the mis-regulated genes were obtained via the Mouse Genome Informatics database (MGI; http://www.informatics.jax.org). Comparative analyses relative to A/B compartments and LADs of ES cells were performed with data obtained from (Bonev et al., 2017; Peric-Hupkes et al., 2010).

Gene Ontology Analysis

Gene ontology enrichment analysis for Cellular Component was performed on the Gene Ontology Consortium website against *Mus musculus* reference list using the PANTHER overrepresentation test (Fisher's Exact test) with False Discovery Rate correction.

Live Imaging

Spinning disk images were acquired at 37°C using a Plan-APO 40x/1.25 NA objective on a Leica DMI6000B microscope enclosed in a thermostatic chamber (Life Imaging Service) equipped with a Retiga 3 CCD camera (QImaging, Burnaby, British Columbia, Canada) coupled to a Sutter filter wheel (Roper Scientific, Trenton, NJ, United States of America) and a Yokogawa CSU-X1-M1 spinning disk. Metamorph software (Universal Imaging, version 7.7.9.0) was used to collect data.

For imaging the nucleus labelled with YFP-Rango, oocytes were illuminated with an excitation wavelength of 491 nm every 500 ms with the stream acquisition mode of Metamorph on one single plane focused on the nucleolus. For imaging chromatin labelled with H2B-RFP, oocytes were illuminated with an excitation wavelength of 561 nm every 500 ms with the stream acquisition mode of Metamorph on one single plane focused on the nucleolus. For RPEL1-GFP-3NLS imaging together with H2B-RFP, images were acquired with a respective excitation wavelength of 491 nm and 561 nm during 500 ms. Z-series were performed with Z-steps of 1 μm. For nAC-GFP imaging together with H2B-RFP, images were acquired with a respective excitation wavelength of 491 nm and 561 nm during 500 ms. Z-series were performed with Z-steps of 1 μm.

The FRAP experiments were done at 37°C on a Nikon Eclipse TL microscope enclosed in a thermostatic chamber equipped with an Evolve EMCCD camera (Photometrics, Tucson, Arizona, United States of America) coupled to a Sutter filter wheel (Roper Scientific) and a Yokogawa CSUX1-A1 spinning disc. FRAP experiments were performed on oocytes expressing the YFP-Rango nuclear probe. For the FRAP routine, an Ilas2 targeted laser illumination system (Roper Scientific) was used. 491 nm full power laser line was activated during 202 ms in bleach point mode with a Plan Apo lambda 60X, N.A: 1.4 (Nikon). 6 mW power at 491 nm was measured at back focal plane. The recovery sequence was realized by acquiring 256x256 pixels images, with 33 ms exposure time at maximum frame rates (30 frames per second), using 10% laser power.

Immunofluorescence

Oocytes were fixed 30 min at 30°C in 4% paraformaldehyde on coverslips treated with gelatin and polylysine. Permeabilization was done by incubating oocytes in 0.5% Triton-X in PBS for 10 min at room temperature. For Lamin A staining, a rabbit monoclonal antibody was used against Lamin A (Abcam, Ref. ab133256) at 1:500 dilution. A Cy3-conjugated secondary antibody (Jackson ImmunoResearch, Ref. 711-165-152) was used at 1:150 dilution. EU detection was carried out following the instructions of the Click-IT RNA Alexa Fluor 488 Imaging kit (Thermofisher, Ref. C10329). DNA was labelled with DAPI in Prolon Gold mounting medium (Thermofisher, Ref. P36941). Oocytes were mounted onto 250 nm thick perforated stickers to avoid smashing of the oocytes (Electron Microscopy Sciences, Hatfield, Pennsylvania, United States of America, Ref. 70366-12).

For Lamin A and DAPI staining, images were acquired using a Leica SP5 confocal microscope with a Plan APO63/1.25NA objective. Z-series were performed with Z-steps of 0.5 μm. For EU signal imaging, images were acquired using a Leica DMI6000B microscope equipped with a Retiga 3 CCD camera (QImaging) coupled to a Sutter filter wheel (Roper Scientific) and a Yokogawa CSU-X1-M1 spinning disk, with a Plan-APO 40x/1.25 NA objective.

Image Analysis

When the shape of nuclei was asymmetric (for *Fmn2*$^{-/-}$ and *Fmn2*$^{+/-}$ + CCD), nuclei labelled with YFP-Rango were rotated on Fiji (Schindelin et al., 2012) to orient the smooth part up and the invagination down, in order to analyse nuclear envelope fluctuations. Then a custom plugin developed for Fiji was used to remove the noise in the signal using the Pure denoise plugin, threshold the signal and fill the hole corresponding to the nucleolus in order to create a binary nucleus mask, realign it, and calculate the distance r from the centroid of the nucleus mask to the circumference of the mask for all θ angles (θ from 0 to 360°by 1° increment, as defined in Figure 2B). Results were provided as xls files. Then, for each nucleus, the mean distance R over all the 600 time points t for each defined θ angle was calculated, allowing to plot the mean shape over time (Figure 2B). For each θ, the mean distance R was subtracted from the distance r for all time points t. The variance $(r-R)^2$ is a measure of nuclear envelope fluctuations. The mean fluctuation of nuclear shape was calculated for all time points t and all angles θ. Eventually, for all nuclei coming from one condition (*Fmn2*$^{+/-}$, *Fmn2*$^{-/-}$, CCD, NZ), the mean of the fluctuations for all time points t and all angles θ was calculated.

Heatmaps representing the mean fluctuations for each defined θ angle over all time points t and plotted along the contour of the mean shape were generated using the G-plot package on R (version 3.3.2).

Fourier transform calculation was done on the fluctuations values (r-R) for all angles θ and all time points t. We used the fft package on R to extract the values of the Fourier transform moduli.

Nucleolus automated tracking was performed on the same movies coming from nuclei labelled with YFP-Rango used to analyse nuclear envelope fluctuations, similarly reoriented with the smooth part up and the invagination down. A custom plugin for Fiji was developed to threshold the signal and fill the hole corresponding to the nucleolus in order to create the binary nucleus mask and realign it. The mask of the nucleolus was then extracted from the realigned nucleus mask, allowing the tracking of the centroid of the nucleolus in the frame of the realigned nucleus. Trajectories were provided as xls files and then converted to xml files for Mean Squared Displacement analysis.

For time projections of chromatin movies labelled with H2B-RFP, the background was subtracted and bleaching was corrected using the Histogram Matching algorithm on Fiji. A sub-stack of 10 planes every 10 s (90 s total duration) was selected and time-projection was done with the Temporal-colour code plugin on Fiji, using a custom LUT.

For Mean Square Displacement analysis of nucleoli trajectories, we used the @msdanalyzer class of MATLAB version 2016a (MathWorks) described in:

http://bradleymonk.com/matlab/msd/MSDTuto.html

Single plane images of nuclei stained for Lamin A and DAPI (Figures 1A and 1D) were done on Fiji.

EU signal analysis was done using Metamorph (Figures S4A and S4B). After subtracting the background, the integrated intensities of EU and DAPI staining were determined in the mid-sectional plane, within the same ROI for both channels for a given oocyte. ROIs of identical areas were used for all oocytes in all conditions. The EU:DAPI ratio was calculated.

RPEL1 and nAC signal analysis (Figure S6) was done on Metamorph. Planes below and above the nucleus were removed from Z-stacks. A sum projection was done on the remaining stacks, and the background was subtracted from the resulting image. The total intensity was calculated in a region, including the nucleus. The same region was used for RPEL1-GFP-3NLS or nAC-GFP and for H2B-RFP.

To determine the nucleo-cytoplasmic ratio of YFP-Rango (Figure S1), after background subtraction, total intensities were determined on Metamorph in 6 circular regions of the same size (2 nuclear and 4 cytoplasmic). The mean of nuclear and cytoplasmic intensities and the corresponding ratio were calculated for each nucleus.

For FRAP analysis, after background subtraction, a circular region of 2-μm diameter, the same as the spot size, was positioned in the region of lowest total intensity in the first frame of the post-bleach sequence. Total intensity in this region was then measured on Metamorph for all the time points of the sequence. In order to be able to compare different experiments, the last pre-bleach time point was normalized to 1. The normalized data curves were corrected for the photo-bleaching occurring during acquisition by dividing the normalized fluorescence by a function modeling photo-bleaching. This function was determined by fitting the fluorescence decay observed in the pre-bleach phase to a mono-exponential function of the type $F(t) = (Fi - Finf)\, e^{-t/\tau} + Finf$, where Fi is the normalized fluorescence intensity at the first pre-bleach time point, Finf is the normalized fluorescence intensity at infinite and τ is the time constant corresponding to the time when 63% of the total photo-bleaching had occurred. Fi, Finf and τ were determined by the fitting.

Computational 3D Imaging

3D Image Segmentation

in order to use of isometric 3D kernels, we performed a straightforward anisotropy correction of the stack of images by performing a cubic interpolation in the z direction. Thus, the interpolated stack of images has equal dimensions on x, y, and z axes. After denoising using a Laplacian filtering (sigma = 3), a robust 3D segmentation of the two channels of the 3D stack image was performed using a k-means clustering of the grey levels and spatial information (Achanta et al., 2012) implemented in the scikit-image python package (version 0.11.3 of Python 2.7). Each channel is split into three clusters. The cluster with the highest intensity corresponds to the foreground object in each channel (Lamin A or DNA). The segmentation algorithm considers a ''compactness'' parameter that balances color. Spatial relationships were set to 0.01 to segment the DNA signal and 0.005 to segment the Lamin A signal properly. The parameter was then maintained unchanged for the whole dataset.

3D Features Extraction

94 quantitative features were extracted from DNA and Lamin A foregrounds to describe the morphological changes for all stacks in all conditions. The full list of features is displayed at the end of this section. Features can be summarized into shape and volume, DNA dispersion, features measuring the overlap between DNA and Lamin A signals, features measuring the isolated and detached pieces of DNA and features measuring spreadness and distances between DNA and Lamin A signals.

Data Analysis

After extracting 3D features on the whole dataset using a computing cluster, each 3D image for each condition was represented by a vector of 94 features. Those data were then analyzed using two approaches:

Univariate data analysis: chosen features were used to compare selected couples of conditions using univariate statistical tests: Mann-Whitney U test (one tailed) with Bonferroni correction when needed.

Multivariate data analysis: Highly correlated features were identified as connected components of a complete weighted correlation graph thresholded at 0.8, and the feature with the maximum of connections on each connected component was selected. This feature selection step retained 46 features listed at the end of this section. Linear Discriminant Analysis (Martinez and Kak, 2001) was then performed on subsets of conditions using the 46 remaining features: each nucleus, now profiled as a 46-dimensional features was projected onto a lower-dimensional space by simultaneously maximizing the inter-class variance and minimizing the intra class variance. The first axis (LD1) of the two-dimensional space, where the 46 features dataset for each oocyte is projected, represents 72% of the variance whereas the second axis (LD2) represents 20% of the variance.

Computational 3D image analysis features:

● Shape and volume features: features were extracted to describe the shape of oocyte nuclei from each stack of images where DNA and Lamin A have been stained. Volumes, convex hulls volumes of DNA and of Lamin A, volumes of fitted ellipsoid to the DNA and to Lamin A signals were computed using the formula (1), the ratio between the volume of the convex hull and the volume of the fitted ellipsoid, the eigenvalues of the Principal Component Analysis (PCA) of the DNA and the Lamin A foregrounds and other shape features (shape factor, aspect ratio, sphericity, and flatness) using the formulas described (Arasan et al., 2010).

$$V = \left(\frac{4}{3}\right) * \pi * a * b * c$$

With a, b, and c respectively the semi-major, the semi-medium and the semi-minor axes of the ellipsoid. They correspond to the eigenvalues of the Principal Component Analysis.

● DNA dispersion features: To study the dispersion of the DNA, the distribution of the distances from the center of mass of the DNA to each segmented voxel of the foreground DNA signal was considered. The mean, the median, the variance, and the standard deviation of the distances were computed.

● Overlap between the DNA and the Lamin A features: to study the contact between Lamin A and DNA signals, the region of overlap was extracted and features were computed. They correspond to the percentage of overlap comparing the DNA foreground signal to the Lamin A foreground signal.

● Isolated and detached pieces of DNA: each isolated and detached piece of DNA represents a connected region and is called a connected component. Each connected component is extracted, and a set of features is measured: its size and its mean intensity. Each 3D stack of images is quantified by the number of connected components for the DNA and a set of statistical features (mean, median, maximum, and variance) representing the sizes and intensities of those connected components.

● Spreading and distances between DNA and Lamin A signals: to measure the spreading of DNA and the distances between DNA and Lamin A signals, the distances from the center of mass to the segmented signal for DNA (dists1) and then the distances from the center of mass to the segmented signal of Lamin A (dists2) are computed. Then a set of relational-based distances features are considered :

$$F1 = |(mean(dists1) - mean(dists2))|$$

$$F2 = var(dists1)/var(dists2)$$

Those features are calculated alternatively using the center of mass of the DNA, the center of mass of the Lamin A and eventually the center of mass of the concatenation of the two signals (DNA and Lamin A). We also consider the euclidean and manhattan distances between the normalized histograms of dists1 and dists2.

$$F3 = Euclideandistance(hist(dists1), hist(dists2))$$

$$F4 = Manhattandistance(hist(dists1), hist(dists2))$$

To compare the two distributions of distances, a t test of two distributions is performed and the p value is considered as a feature.

$$F5 = pvalue(dists1, dists2)$$

The dataset is made of 140 stack images acquired for conditions summarized here:

Condition or Oocyte Class	Number of Oocytes
Fmn2$^{+/-}$	35
Fmn2$^{-/-}$	24
Fmn2$^{-/-}$ + Fmn2	26
Fmn2$^{-/-}$ + FH1-FH2	23
Fmn2$^{-/-}$ + Nter	32

The 94 features computed for each oocyte nucleus reconstituted in 3D:

Feature id	Feature Description
Feature 1	mean intensity of the segmented Lamin A voxels
Feature 2	median intensity of the segmented Lamin A voxels
Feature 3	variance of the intensity of the segmented Lamin A voxels
Feature 4	first eigenvalue (λ1) of the segmented Lamin A voxels
Feature 5	second eigenvalue (λ2) of the segmented Lamin A voxels
Feature 6	third eigenvalue (λ3) of the segmented Lamin A voxels
Feature 7	$\frac{\lambda 1}{\lambda 1+\lambda 2+\lambda 3}$ (for segmented Lamin A)
Feature 8	$\frac{\lambda 2}{\lambda 1+\lambda 2+\lambda 3}$ (for segmented Lamin A)
Feature 9	$\frac{\lambda 3}{\lambda 1+\lambda 2+\lambda 3}$ (for segmented Lamin A)
Feature 10	$\lambda 1 * \lambda 2 * \lambda 3$ (for segmented Lamin A)
Feature 11	$\frac{\lambda 1+\lambda 2+\lambda 3}{3}$ (for segmented Lamin A)
Feature 12	$\frac{\lambda 3}{\sqrt{\lambda 1 * \lambda 2}}$ (for segmented Lamin A)
Feature 13	$\frac{\lambda 1}{\lambda 2}$ (for segmented Lamin A)
Feature 14	$\sqrt[3]{\frac{(\lambda 2 * \lambda 3)}{\lambda 1^2}}$ (for segmented Lamin A)
Feature 15	$\frac{\lambda 3}{\lambda 2}$ (for segmented Lamin A)
Feature 16	volume of the largest connected component (CC) formed by the segmented Lamin A voxels
Feature 17	variance of the CC volumes from Lamin A
Feature18	mean CC volume from Lamin A
Feature19	median CC volume from Lamin A
Feature 20	mean volume of the Lamin A CCs larger than the average Lamin A CC volume
Feature 21	median volume of the Lamin A CCs larger than the average Lamin A CC volume
Feature 22	maximum of the Lamin A CCs mean intensities
Feature 23	mean of the Lamin A CCs mean intensities
Feature 24	median of the Lamin A CCs mean intensities
Feature 25	maximum of the Lamin A CCs intensity variances
Feature 26	mean of the Lamin A CCs intensity variances
Feature 27	variance of the Lamin A CCs intensity variances
Feature 28	mean intensity of the segmented DNA voxels
Feature 29	median intensity of the segmented DNA voxels
Feature 30	variance intensity of the segmented DNA voxels
Feature 31	maximum of the distances from the center of mass and the voxels of the segmented DNA voxels (corresponding also to the radius of the enclosing sphere)
Feature 32	sum of the distances from the center of mass and the segmented DNA voxels
Feature 33	mean of the distances from the center of mass and the segmented DNA voxels
Feature 34	median of the distances from the center of mass and the segmented DNA voxels
Feature 35	variance of the distances from the center of mass and the segmented DNA voxels
Feature 36	first eigenvalue ($\Lambda 1$) of the segmented DNA voxels
Feature 37	second eigenvalue ($\Lambda 2$) of the segmented DNA voxels
Feature 38	third eigenvalue ($\Lambda 3$) of the segmented DNA voxels

(*Continued on next page*)

Continued

Feature id	Feature Description
Feature 39	$\frac{\Lambda 1}{\Lambda 1+\Lambda 2+\Lambda 3}$ (for segmented DNA)
Feature 40	$\frac{\Lambda 2}{\Lambda 1+\Lambda 2+\Lambda 3}$ (for segmented DNA)
Feature 41	$\frac{\Lambda 3}{\Lambda 1+\Lambda 2+\Lambda 3}$ (for segmented DNA)
Feature 42	$\Lambda 1 * \Lambda 2 * \Lambda 3$ (for segmented DNA)
Feature 43	$\frac{\Lambda 1+\Lambda 2+\Lambda 3}{3}$ (for segmented DNA)
Feature 44	$\frac{\Lambda 3}{\sqrt{\Lambda 1 * \Lambda 2}}$ (for segmented DNA)
Feature 45	$\frac{\Lambda 1}{\Lambda 2}$ (for segmented DNA)
Feature 46	$\sqrt[3]{\frac{(\Lambda 2 * \Lambda 3)}{\Lambda 1^2}}$ (for segmented DNA)
Feature 47	$\frac{\Lambda 3}{\Lambda 2}$ (for segmented DNA)
Feature 48	maximum CC volume of the segmented DNA voxels
Feature 49	variance of the CC volume of the segmented DNA voxels
Feature 50	mean CC volume of the segmented DNA voxels
Feature 51	mean volume of the DNA CCs larger than the average DNA CC volume
Feature 52	median volume of the DNA CCs larger than the average DNA CC volume
Feature 53	mean of the DNA CCs mean intensities
Feature 54	median of the Lamin A CCs mean intensities
Feature 55	maximum of the Lamin A CCs intensity variances
Feature 56	mean of the Lamin A CCs intensity variances
Feature 57	median of the Lamin A CCs intensity variances
Feature 58	number of segmented DNA voxels
Feature 59	number of segmented Lamin A voxels
Feature 60	ratio between the number of segmented DNA voxels and the number of segmented Lamin A voxels
Feature 61	volume of the segmented signal of DNA (in μm^3)
Feature 62	volume of the segmented signal of Lamin A (in μm^3)
Feature 63	ratio between the volume of the segmented signal of DNA and the volume of the segmented signal of Lamin A
Feature 64	volume of an ellipsoid fitted to the segmented DNA voxels computed using formula (1)
Feature 65	volume of an ellipsoid fitted to the segmented Lamin A voxels computed using formula (1)
Feature 66	volume of the convex hull of the segmented DNA voxels
Feature 67	surface of the convex hull of the segmented DNA voxels
Feature 68	volume of the convex hull of the segmented Lamin A voxels
Feature 69	surface of the convex hull of the segmented Lamin A voxels
Feature 70	ratio between the volume of the convex hull and the volume of an ellipsoid fitted to the segmented DNA voxels
Feature 71	ratio between the volume of the convex hull and the volume of an ellipsoid fitted to the segmented Lamin A voxels
Feature 72	ratio between the volume of overlapping region and the volume of the Lamin A
Feature 73	ratio between the volume of the Lamin A and DNA overlapping region and the volume of DNA
Feature 74	mean of intensity of the Lamin A on the Lamin A and DNA overlapping region

(*Continued on next page*)

Continued

Feature id	Feature Description
Feature 75	median of intensity of the Lamin A on the Lamin A and DNA overlapping region
Feature 76	variance of intensity of the Lamin A on the Lamin A and DNA overlapping region
Feature 77	mean of intensity of the DNA on the Lamin A and DNA overlapping region
Feature 78	median of intensity of the DNA on the Lamin A and DNA overlapping region
Feature 79	variance of intensity of the DNA on the Lamin A and DNA overlapping region
Feature 80	number of connected components for the segmented Lamin A signal
Feature 81	number of connected components for the segmented DNA signal
Feature 82	$F1 = \lvert(mean(dists1) - mean(dists2))\rvert$ with Lamin A center of mass
Feature 83	$F2 = var(dists1)/var(dists2)$ with Lamin A center of mass
Feature 84	$F3 = Euclideandistance(hist(dists1), hist(dists2))$ with Lamin A center of mass
Feature 85	$F4 = Manhattandistance(hist(dists1), hist(dists2))$ with Lamin A center of mass
Feature 86	$F1 = \lvert(mean(dists1) - mean(dists2))\rvert$ with DNA center of mass
Feature 87	$F2 = var(dists1)/var(dists2)$ with DNA center of mass
Feature 88	$F3 = Euclideandistance(hist(dists1), hist(dists2))$ with DNA center of mass
Feature 89	$F4 = Manhattandistance(hist(dists1), hist(dists2))$ with DNA center of mass
Feature 90	$F1 = \lvert(mean(dists1) - mean(dists2))\rvert$ using center of mass of the concatenation of the two signals (DNA and Lamin A)
Feature 91	$F2 = var(dists1)/var(dists2)$ using center of mass of the concatenation of the two signals (DNA and Lamin A)
Feature 92	$F3 = Euclideandistance(hist(dists1), hist(dists2))$ using center of mass of the concatenation of the two signals (DNA and Lamin A)
Feature 93	$F4 = Manhattandistance(hist(dists1), hist(dists2))$ using center of mass of the concatenation of the two signals (DNA and Lamin A)
Feature 94	$F5 = pvalue(dists1, dists2)$ using center of mass of the concatenation of the two signals (DNA and Lamin A)

The list of 46 remaining features after selection are : 1, 5, 6, 8, 9, 14, 15, 16, 17, 18, 20, 22, 25, 31, 33, 35, 37, 38, 40, 41, 42, 46, 47, 49, 50, 51, 52, 53, 58, 59, 60, 65, 66, 68, 70, 71, 72, 73, 75, 76, 79, 80, 81, 83, 91, 92.

Bio-Physical Model

In this section, we present theoretical arguments to support the mechano-transduction model proposed in the main text. We show that F-actin dependent cytoplasmic activity generates non-thermal fluctuations of the nuclear envelope, which in turn significantly enhance chromatin diffusion.

The oocyte cytoplasm can be modelled as an active fluid (Almonacid et al., 2015). Here the term "active" refers to non-equilibrium processes (i.e. ATP dependent) involving F-actin, such as polymerisation/depolymerisation of actin filaments or actin/Myosin V interactions. We do not aim at modelling accurately these processes at the microscopic scale: indeed, at time scales larger than a microscopic correlation time, they can be effectively modelled as a Gaussian white noise, so that we eventually describe the cytoplasm as an active bath of effective temperature $T_{cyto} = T + Ta$, where T is the usual temperature and the active temperature T_a accounts force the fluctuations of the F-actin network. The rheology of the nuclear envelope being largely unknown, we adopt the classical Helfrich model of membranes (Nelson et al., 1989), parametrized by a tension $\overline{\sigma}$ and a bending modulus $\overline{\kappa}$. In order to compare the model to experimentally accessible data, we consider only radial deformations of the envelope in a 2D projection plane, and parametrize the envelope by its local radial deformation $h(\theta,t) = r(\theta,t) - R(\theta)$, where $R(\theta)$ is the average over time of the radial coordinate $r(\theta,t)$ of the envelope at the angle θ. The fluctuations of the envelope are then conveniently analyzed by introducing the Fourier decomposition

$$\widehat{h}_n = \int_0^{2\pi} e^{-in\theta} h(\theta) d\theta \qquad \text{(Equation 1)}$$

The effective Helfrich Hamiltonian of a given 2D projected configuration can then be expressed in Monge representation by

$$H = \int_0^{2\pi} \left\{ \frac{1}{2}\overline{\sigma}\left(\frac{\partial h}{\partial \theta}\right)^2 + \frac{1}{2}\overline{\kappa}\left(\frac{\partial^2 h}{\partial \theta^2}\right)^2 \right\} d\theta \qquad \text{(Equation 2)}$$

where $\overline{\sigma} \propto \sigma$ is the effective tension and $\overline{\kappa} \propto \kappa/R^2$ the effective bending modulus after projection, with R the mean nucleus radius. Making use of the fluctuation dissipation theorem, the power spectrum of fluctuations is then deduced and can be written

$$|\widehat{h}_n|^2 = \frac{2\pi k_B T_{cyto}}{\bar{\sigma} n^2 + \bar{\kappa} n^4}, \qquad \text{(Equation 3)}$$

where k_B is the Boltzmann constant.

This prediction shows that nuclear envelope fluctuations (quantified by the power spectrum) are controlled by the activity of the cytoplasm, which is here quantified by the active temperature T_a. This can be compared to experimental data. Importantly, all power spectra obtained experimentally (*Fmn2*$^{+/-}$, *Fmn2*$^{-/-}$, CCD- and NZ-treated oocytes) could be fitted by Equation 3, indicating the relevance of the Helfrich model to describe nuclear envelope fluctuations. The fitting procedure gives access in particular to the characteristic length $l_c = R\sqrt{\bar{\kappa}/\bar{\sigma}}$, which is a marker of the physical properties of the nuclear envelope (note that the determination of tension and bending modulus independently is not accessible by this approach). Our analysis reveals that l_c took close values (in the range 0.24-0.4 μm) in *Fmn2*$^{+/-}$, *Fmn2*$^{-/-}$ and CCD-treated oocytes (see Table 1). This suggests that the physical properties of the nuclear envelope are comparable in all cases and that the observed differences of power spectra are due mainly to differences in activity of the cytoplasm. More quantitatively, this analysis indicates that the power spectra of *Fmn2*$^{-/-}$ and CCD treated oocytes display effective temperatures T_{cyto} that are 5 times lower than *Fmn2*$^{+/-}$ oocytes. Overall, this strongly suggests that the observed nuclear envelope fluctuations are generated by Formin 2-induced cytoplasmic activity and are not due to inherent changes of nuclear envelope properties in the different types of oocytes.

Last, we argue that the active fluctuations of the nuclear envelope lead to an increased effective temperature of the nucleoplasm, and therefore to an enhanced diffusion of the chromatin. The experimental observation that chromatin performs Brownian diffusion (as indicated by a mean squared displacement linear in time) suggests that the nucleoplasm can be described as a viscous fluid. We then write the following Langevin equation for the dynamics of the nucleolus of position x in the nucleus

$$\lambda \frac{dx}{dt} = \xi_L + \xi_a$$

where ξ_L is Langevin force characterized by $\xi_L(t)\xi_L(t') = 2\lambda k_B T \delta(t - t')$, with the friction λ and temperature T.

In turn, ξ_a is the active force induced by the active fluctuations of the nuclear envelope, and transduced by the nucleoplasm treated as a viscous fluid. At sufficiently large time scales, dimensional analysis suggests that the corresponding correlation function can be written $\xi_a(t)\xi_a(t') = 2\lambda k_B \alpha T_a \delta(t - t')$, where T_a is the active temperature of the cytoplasm that controls nuclear envelope fluctuations and α<1 is a numerical constant that accounts for the dampening of these active forces in the nucleus. This finally shows that the nucleolus performs Brownian diffusion in a fluid of effective temperature $T_{nuc} = T + \alpha T_a$, which is increased by the cytoplasmic activity, leading to a higher diffusion coefficient $D = k_B(T + \alpha T_a)/\lambda$. This analysis is in agreement with observations, which shows that the diffusion coefficient of the nucleolus (and therefore the corresponding effective temperature) is 3 times larger for *Fmn2*$^{+/-}$ oocytes than for *Fmn2*$^{-/-}$ oocytes.

Non-linear Fitting of Fourier Transforms

For each nucleus, squared values of Fourier transform moduli were averaged for each mode over all time points t. Data were fitted to the function 1 / ($\bar{\sigma}n^2 + \bar{\kappa}n^4$) + Yinf according to the Helfrich model. The additional off-set parameter Yinf was introduced to take into account the background high-frequency noise in the data of the power spectrum. Data processing and fitting were done using the open source software R. For each nucleus, data were linearly interpolated using the function "approx", for values of θ from 2° to 180°. Interpolated data were then averaged for each condition (*Fmn2*$^{+/-}$, *Fmn2*$^{-/-}$, CCD, NZ). The model was eventually fitted to the average data with the Marquardt method using the function "nlsLM" of the R package minpack.lm. Data for modes < 5 and > 178 were not considered for the fit due to missing values, except for *Fmn2*$^{+/-}$ oocytes. Squared values of Fourier transform moduli, averaged, and predicted from the fitted model, where then exported as .csv files and plotted with Microsoft Excel.

QUANTIFICATION AND STATISTICAL ANALYSIS

Mann-Whitney tests with Bonferroni correction were performed with Python 2.7 using the scipy.stats library (one-tailed tests) or with the GraphPad Prism software v 7.0 (two-tailed tests). Two-tailed student t tests were performed with Python or with Prism. One-way ANOVA followed by Tukey's multiple comparison tests for ratios was performed with Prism. Fits of MSDs data were done with R. All statistical details can be found in the figure legends.

DATA AND CODE AVAILABILITY

The RNA-seq data that support the findings of this study have been deposited in the Gene Expression Omnibus with the accession number GEO: GSE103718.

For 3D computational analysis of nuclear architecture, all code needed to reproduce the results can be found at https://github.com/biocompibens/Meiospin.

For analysis of nuclear envelope fluctuations and tracking of the nucleoli, the code can be found at https://github.com/pmailly/Ovocyte_Nucleus_Analyze.